Stability of crystalline solids—II: Application to temperature-induced martensitic phase transformations in a bi-atomic crystal

Ryan S. Elliott[*,1], John A. Shaw, Nicolas Triantafyllidis

Department of Aerospace Engineering, University of Michigan, Ann Arbor, MI 48109, USA

Abstract

This paper applies the stability theory of crystalline solids presented in the companion paper (Part I) to the study of martensitic transformations found in shape memory alloys (SMA's). The focus here is on temperature-induced martensitic transformations of bi-atomic crystals under stress-free loading conditions. A set of temperature-dependent atomic potentials and a multilattice description are employed to derive the energy density of a prototypical SMA ($B2$ cubic austenite crystal). The bifurcation and stability behavior are then investigated with respect to two stability criteria (Cauchy–Born (CB) and phonon). Using a 4-lattice description five different equilibrium crystal structures are predicted: $B2$ cubic, $L1_0$ tetragonal, $B19$ orthorhombic, $Cmmm$ orthorhombic, and $B19'$ monoclinic. For our chosen model only the $B2$ and $B19$ equilibrium paths have stable segments which satisfy both the CB- and phonon-stability criteria. These stable segments overlap in temperature indicating the possibility of a hysteretic temperature-induced proper martensitic transformation. The $B2$ and $B19$ crystal structures are common in SMA's and therefore the simulated jump in the deformation gradient at a temperature for which both crystals are stable is compared to experimental values for NiTi, AuCd, and CuAlNi. Good agreement is found for the two SMA's which have cubic to orthorhombic transformations (AuCd and CuAlNi).
© 2005 Elsevier Ltd. All rights reserved.

Keywords: Phase transformation; Finite strain; Stability and bifurcation; Asymptotic analysis

[*]Corresponding author.

E-mail address: elliott@aem.umn.edu (R.S. Elliott).

[1]Current address: Department of Aerospace Engineering and Mechanics, University of Minnesota, Minneapolis, MN 55455, USA.

1. Introduction

The stability theory of crystalline solids using multilattice kinematics has been discussed in the companion paper Elliott et al. (2004b) (henceforth referred to as Part I), where three different stability criteria were presented and compared. Here an application of this theory to martensitic transformations that occur in shape memory alloys (SMA's) is considered. As a first step, the focus is on temperature-induced martensitic transformations under stress-free loading conditions.

Martensitic transformations (MT's) according to Cohen et al. (1979) are diffusionless lattice-distortive phase transformations of the crystal. That is, during a martensitic transformation the atoms of a highly ordered crystal rearrange in a coordinated manner leading to a new crystalline phase. These transformations are often temperature-induced and may occur over a wide range of temperatures. The high temperature phase is called *austenite* and the low temperature phase is called *martensite*. In the materials science literature MT's are often further subdivided into those which are reversible (or thermo-elastic) as for SMA's and those which are irreversible as for martensitic steels.

Here a somewhat different view is adopted, as proposed in Elliott et al. (2002b), where MT's are partitioned into two categories called *proper MT's* and *reconstructive MT's*. Proper MT's are identified by the austenite and martensite crystals having a group-subgroup symmetry relationship. This has been shown to be a necessary feature for a material to exhibit a shape memory effect (see Bhattacharya, 2003), since it guarantees that austenite is a unique configuration to which martensite can revert. Additionally, if high symmetry austenite and low symmetry martensite configurations are connected by an infinitesimal deformation, the so-called Ericksen–Pitteri neighborhood (Ericksen, 1978; Pitteri, 1984; Bhattacharya, 2003), the phase transformation is likely to be reversible upon cooling or heating in some neighborhood of the transformation temperature. In a reconstructive MT, by contrast, no group–subgroup relationship exists between the crystal configurations. Although not considered diffusional, the transformation involves significant atomic motions with breaking of nearest-neighbor bonds and then bond reformation (Tolédano and Dmitriev, 1996), often resulting in significant dilatational changes of the crystal. Reconstructive MT's exist in many materials, including steel, many of the pure elements, and ionic compounds such as CsCl, NaCl, and other alkali-halides. Reconstructive MT's were successfully simulated in Elliott et al. (2002b), where a set of temperature-dependent Morse pair-potentials were used to investigate the uniform (affine) deformation of a bi-atomic $B2$ crystal structure, and an MT between the cubic $B2$ and cubic $B1$ crystal structures was simulated.

Martensitic transformations have been a subject of active study for many decades. In 1937 *L. D. Landau* developed a phenomenological theory of phase transitions including MT's (see, for example, Dove, 1993). This theory has successfully modeled the properties of known phase transitions (see, for example, Bruce and Cowley, 1981; Dove, 1993). In Landau theory the "free energy" of the crystal is expanded as a polynomial function with temperature-dependent coefficients of an "order parameter" that measures the extent of transformation. The form of the free energy is constrained to satisfy certain symmetry relations for the crystal of interest. Phase transformation is assumed to occur at the temperature where the free energy of the austenite phase becomes equal to the free energy of the martensite phase.

Many researchers have developed *continuum-level* models for SMA's by working with mixture theories to describe the material's behavior. Notable treatments include Tanaka (1986), Brinson (1993), Sun and Hwang (1993), Boyd and Lagoudas (1994), Patoor et al. (1996), Levitas (1998), and Hall and Govindjee (2002). One of the first to investigate stress-induced material instabilities was Ericksen (1975), who considered one-dimensional bars with non-monotonic stress-strain curves. Others have considered the strain localization behavior often observed in SMA's (see, for example, Shaw and Kyriakides, 1995, 1997) and formulated SMA models based on thermodynamics and a set of postulated kinetic relations for the propagation of localized transformation fronts. For example, the works of Abeyaratne and Knowles (1993), Leo et al. (1993), Vainchtein (1999), Ngan and Truskinovsky (1999), and Shaw (2002) all take this approach in one form or another. Each of the SMA material models mentioned above addresses some aspects of macroscopic SMA behavior, but they cannot answer some fundamental questions of material behavior at the atomic scale, thus motivating the present three-dimensional lattice investigation.

The macroscopic behavior of SMA's is intimately tied to the fine needle-like martensite *microstructures* that develop in these materials, and a large literature now exists to help explain phenomena at this scale. Successful continuum approaches that take into account the different martensite variants and their possible spatial arrangements have been investigated by James (1986), Bhattacharya (1991), Chu and James (1995), Hane and Shield (1999), Saxena et al. (2003), and Ahluwalia et al. (2004). These methods are based on a global energy minimization that predicts a sequence of fine microstructures. One of these energy based methods is reviewed in the recent book by Bhattacharya (2003). Despite the success of these efforts, their continuum nature leaves many questions regarding the material's martensitic transformation unanswerable.

At the *molecular scale* researchers such as Yu and Clapp (1989), Shao et al. (1996), Grujicic and Dang (1995), and Kastner (2003), have applied molecular dynamics (MD) methods to the atomistic study of SMA's providing valuable insight into the elastic properties of the SMA, the dynamic behavior of atoms in the crystal, and the mechanisms leading to initiation and propagation of phase transformation. However, MD simulations provide information only about stable equilibrium configurations with little indication as to the material's behavior away from these states. Additionally, such investigations are quite computationally intensive. Charlotte and Truskinovsky (2002) have conducted a complete investigation of finite one-dimensional crystals with next-nearest-neighbor atomic interactions and discussed the effects of finite size on the equilibrium solutions and their stability.

At a more fundamental level, researchers including Fukuda et al. (1999) and Huang et al. (2002) have performed quantum mechanics calculations to determine the total internal energy (at $0\,K$) associated with the observed SMA crystal structures (phases). These results provide information about the relative thermodynamic stability of the phases, but only at $0\,K$.

In our previous work, Elliott et al. (2002b), the material's continuum energy density is explicitly derived from a set of phenomenological atomic interaction potentials. This conveniently brings the problem of finding the equilibrium phases as a function of temperature into the realm of bifurcation and stability theory. The bifurcation approach to studying crystal phase transformations has been pioneered by Ericksen (1992), whose extensive work on the topic has recently been collected in the volume edited by Beatty and Hayes (2005).

In contrast to the MD method, a bifurcation and stability analysis systematically determines both stable and unstable equilibrium configurations, providing additional information about equilibrium paths connecting different phases. Furthermore, unstable bifurcating equilibrium paths can eventually become stable away from their initial bifurcation point. Investigating these materials at the atomic length-scale opens many possible avenues for further study, such as clarifying the mechanisms responsible for atomic level instabilities at all length-scales, exploring how MT's interact with defects, precipitates, and grain boundaries, and perhaps even understanding atomic scale mechanisms that identify which alloys can be SMA's and which cannot.

In the current work the kinematic assumptions made in Elliott et al. (2002b) are relaxed to allow multilattice shifts (as discussed in Part I) in order to predict proper MT's of the type seen in SMA's. Additionally, the recommended stability criteria of Part I, (phonon and Cauchy–Born (CB), are employed. Section 2 reviews the multilattice and CB kinematics concepts. Section 3 presents the bifurcation and stability problem of interest, outlines the stability criteria from Part I, and discusses the analytical and numerical techniques to be used. Section 4 investigates a 2-lattice description of the $B2$ crystal structure determining all connected equilibrium paths and their stability and shows that upon cooling short wavelength phonon modes (normal atomic vibration modes) are the first to become unstable. These unstable modes of deformation lead to the consideration of a 4-lattice description of the $B2$ crystal, which is the subject of Section 5. All connected equilibrium paths and their stability are determined, and a proper MT between the $B2$ and $B19$ crystal structures is predicted and results compare favorably with experimental data for AuCd and CuAlNi.

2. Crystal structure description and kinematics

An ordered crystalline solid consists of a periodic arrangement of atoms that has translational symmetry of the crystal at a distance comparable to the atomic separation. This structure can mathematically be described as a lattice, and the particular arrangement of atoms within the lattice gives rise to various point and space group symmetries that can have a profound effect on the microscopic and macroscopic properties of the material (see, for example, Sands, 1993; Nye, 1985; Miller, 1972).

2.1. Multilattices

An M-lattice (see Fig. 1 for an example of a two-dimensional 4-lattice) consists of a set of M inter-penetrating "sub-lattices" each of which is positioned relative to an imaginary "skeletal lattice" (see further, Pitteri and Zanzotto, 2002). Alternatively, a multilattice may be imagined as a set of "motifs", a collection of atoms, or unit cells, with some specified arrangement, located at the lattice points of a Bravais-lattice (skeletal-lattice). The arrangement of atoms about each lattice point is specified by a set of $3M$ quantities $\mathbf{P}[\alpha]$ $\alpha = 0, 1, 2, \ldots, M - 1$; called the "fractional position vectors", as depicted in Fig. 1. A more detailed discussion of the multilattice concept is presented in Part I.

In either view, each atom in the crystal is uniquely identified by specifying the sub-lattice α and lattice point ℓ. The reference position vector of each atom is uniquely
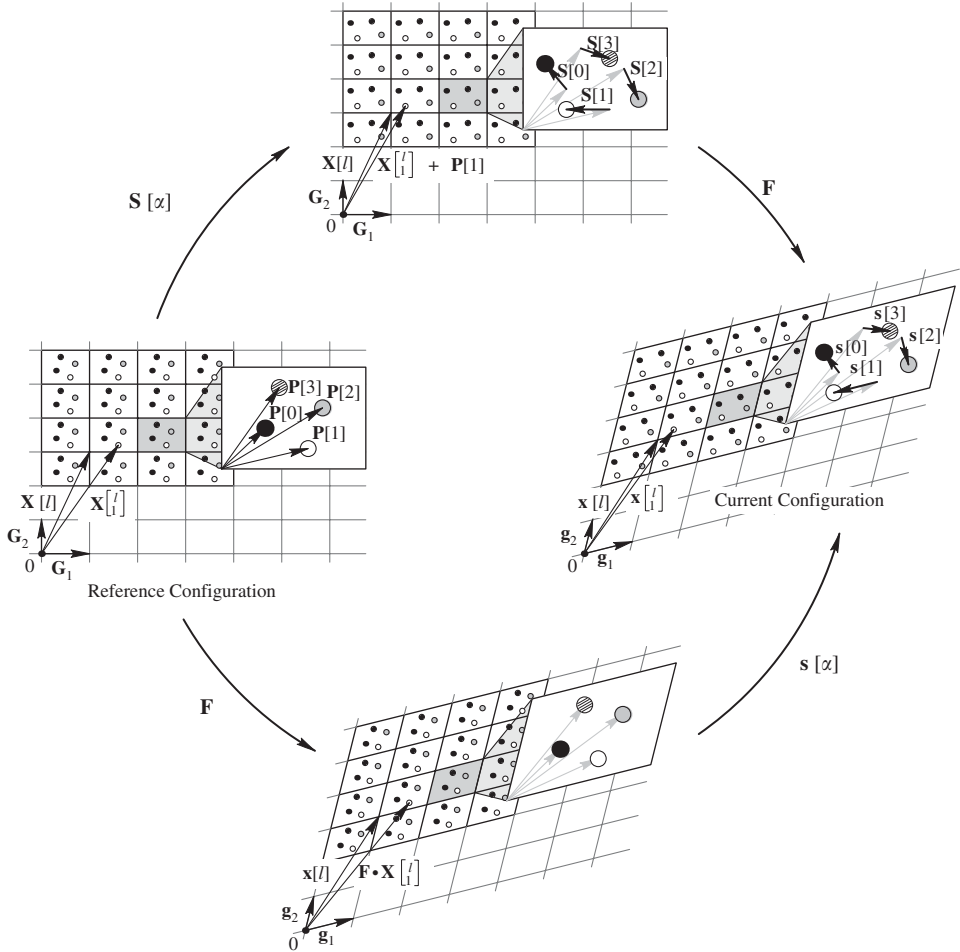
Fig. 1. CB kinematics: Lagrangian (upper path) and Eulerian (lower path) description of shifts leading to the current configuration of a 2-D, 4-lattice crystal.

defined by[1]

$$\mathbf{X}\begin{bmatrix} \ell \\ \alpha \end{bmatrix} = \mathbf{X}[\ell] + \mathbf{P}[\alpha],$$

$$\mathbf{X}[\ell] \equiv \ell^i \mathbf{G}_i, \quad \ell^i \in \mathbb{Z},$$
$$\mathbf{P}[\alpha] \equiv P^i[\alpha]\mathbf{G}_i, \quad 0 \leqslant P^i[\alpha] < 1; \ \alpha = 0, \ldots, M-1; \tag{2.1}$$

where $\mathbf{X}[\ell]$ is the reference position of the skeletal lattice point ℓ, and $\mathbb{Z}$ is the set of all (positive and negative) integers. The label ℓ for the skeletal lattice point is a short-hand notation referring to the triplet of integers ℓ^i, $\mathbf{P}[\alpha]$ is the fractional position vector for atom

---

[1]Unless otherwise specified, Latin indices represent spatial tensor components and Einstein's summation convention is employed.

α, and $\mathbf{G}_i$ are the reference lattice vectors (see again Fig. 1). The reciprocal reference lattice vectors $\mathbf{G}^i$ are defined by[2]

$$\mathbf{G}^i \cdot \mathbf{G}_j = \delta^i_j \quad \text{(Kroneker delta)}, \tag{2.2}$$

and the associated covariant and contravariant components of the metric tensor are

$$G_{ij} \equiv \mathbf{G}_i \cdot \mathbf{G}_j, \quad G^{ij} \equiv \mathbf{G}^i \cdot \mathbf{G}^j. \tag{2.3}$$

2.2. CB kinematics

In this section *quasi-uniform* deformations that take an *M*-lattice into another *M*-lattice are considered. These deformations can be expressed in terms of CB kinematics (see Bhattacharya, 2003; Ericksen, 1984; Born and Huang, 1962), consisting of a uniform deformation $\mathbf{F}$ of the lattice vectors and a set of internal shift vectors $\mathbf{S}[\alpha]$ corresponding to translations of the sub-lattices. CB kinematics can be formulated in either of two ways as shown in Fig. 1, where the upper path corresponds to the Lagrangian formulation, Eq. (2.4) below, and the lower path represents the Eulerian formulation, Eq. (2.5) below, of the shift DOFs. In the Lagrangian formulation, the internal shifts $\mathbf{S}[\alpha]$ are first applied to the reference configuration, and then the uniform deformation $\mathbf{F}$ is applied to this intermediate configuration. The current position vector of an atom $\begin{bmatrix} \ell \\ \alpha \end{bmatrix}$ in this case is

$$\mathbf{x}\begin{bmatrix} \ell \\ \alpha \end{bmatrix} = \mathbf{F} \cdot \left(\mathbf{X}\begin{bmatrix} \ell \\ \alpha \end{bmatrix} + \mathbf{S}[\alpha] \right), \tag{2.4}$$

having a component form $x^i\begin{bmatrix} \ell \\ \alpha \end{bmatrix} = F^i_j (X^j\begin{bmatrix} \ell \\ \alpha \end{bmatrix} + S^j[\alpha])$, with respect to the reference lattice basis vectors $\mathbf{G}_i$. In the Eulerian formulation, the uniform deformation is applied first, followed by the internal shifts:

$$\mathbf{x}\begin{bmatrix} \ell \\ \alpha \end{bmatrix} = \mathbf{F} \cdot \mathbf{X}\begin{bmatrix} \ell \\ \alpha \end{bmatrix} + \mathbf{s}[\alpha]. \tag{2.5}$$

Introducing the current lattice basis vectors

$$\mathbf{g}_i \equiv \mathbf{F} \cdot \mathbf{G}_i, \tag{2.6}$$

the current position vector Eq. (2.5) has components $x^i\begin{bmatrix} \ell \\ \alpha \end{bmatrix} = X^i\begin{bmatrix} \ell \\ \alpha \end{bmatrix} + s^i[\alpha]$, with respect to $\mathbf{g}_i$. That is, the components of the current position vector of atom $\begin{bmatrix} \ell \\ \alpha \end{bmatrix}$ in the Eulerian formulation are the sum of its reference position vector components and the current internal shift components.

These two different forms of CB kinematics Eqs. (2.4) and (2.5) are equivalent, and the current internal shifts are related to the reference internal shifts by

$$\mathbf{s}[\alpha] = \mathbf{F} \cdot \mathbf{S}[\alpha]. \tag{2.7}$$

Each description has its advantages. For example, the Lagrangian formulation Eq. (2.4) provides a more intuitive description of the current configuration of a deformed crystal structure, and therefore, it is used in the numerical investigations of Sections 4 and 5. In

---

[2]Here, (•) indicates tensor contraction of the corresponding vectors.

contrast, the Eulerian formulation Eq. (2.5) is better suited for theoretical investigations due to the absence of coupling between $\mathbf{F}$ and $\mathbf{s}[\alpha]$, and was therefore used in the analytical calculations of crystal stability in Part I.

CB kinematics, Eq. (2.4) or (2.5), include all rigid-body motions of the crystal. For stability evaluations, however, a set of kinematics for which rigid-body modes have been eliminated is required. The following additional constraints are added:

$$\mathbf{F} \equiv \mathbf{U}, \quad \mathbf{S}[0] \equiv \mathbf{0}, \tag{2.8}$$

where $\mathbf{U}$ is the symmetric right stretch tensor. Eq. $(2.8)_1$ eliminates rigid-body rotations from the CB kinematics and is equivalent to setting $\mathbf{R}$, the rotation part of the polar decomposition $\mathbf{F} = \mathbf{R} \cdot \mathbf{U}$, to the identity. Eq. $(2.8)_2$ eliminates rigid-body translations of the crystal by fixing one of the sub-lattices in space. This restricted form of CB kinematics represents a total of $3M + 3$ degrees of freedom (DOFs), six DOFs corresponding to the components of $\mathbf{U}$ and another $3M - 3$ DOFs for the $M - 1$ remaining internal shift vectors $\mathbf{S}[\alpha]$.

3. Problem statement

Stress-free temperature-induced transformations are studied as a first step in modeling martensitic transformations. In particular, the bifurcation and stability properties of the prevalent SMA austenite $B2$ crystal structure (as in NiTi) subjected to temperature changes are presently considered. The $B2$ crystal structure is a 2-lattice, consisting of two simple-cubic sub-lattices arranged so that atoms of one type are symmetrically surrounded by eight atoms of the second type (see Fig. 2). The material is modeled using temperature-dependent atomic pair-potentials with CB kinematics. The objective is to determine all connected equilibrium paths and their stability as a function of temperature, the loading parameter. Special attention is paid to loss of stability of the high symmetry parent phase (austenite) in favor of lower symmetry phases (martensite) upon cooling.
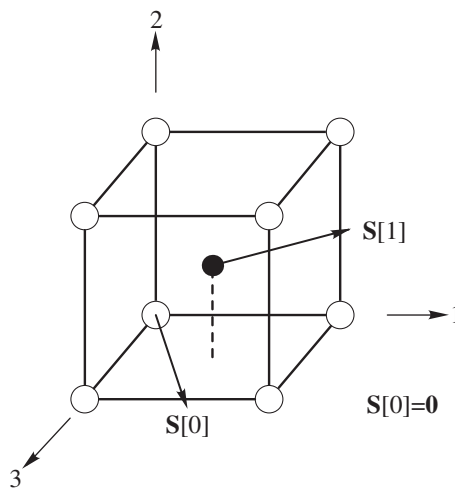

Fig. 2. $B2$ cubic crystal structure (2-lattice).

It is recognized that a "first principles" treatment of finite temperature effects in crystals involves finding the vibrational energy spectrum and evaluating the statistical sum leading to a computation of the free energy and entropy. Commonly, a "mean-field" approach, such as the pseudo-harmonic approximation, is used to obtain a "renormalization" of the phonon frequencies (vibrational energy spectra) with an *explicit* dependence on temperature (Dove, 1993). This is equivalent to a set of "effective", temperature-dependent, atomic potentials. It is in this spirit that we propose the use of a set of purely phenomenological temperature-dependent atomic pair-potentials.

3.1. Atomic potentials

A large number of atomic interaction potentials have been developed for use in molecular-statics and -dynamics simulations. These include relatively simple pair-potential forms such as the *Morse potential*, the *Lennard–Jones potential*, and the *Buckingham potential* (Torrens, 1972). More sophisticated potentials, taking account of non-central forces, include *embedded atom potentials*, *cluster potentials*, and *cluster functionals* (see Carlsson, 1990, for a recent review).

The general methodology introduced in this paper is applicable to any type of atomic potential. For computational speed, pair-potentials are used in the numerical results shown later. Although there are well-known deficiencies associated with the use of pair-potentials, e.g., the Cauchy relations, they are well suited for illustrative purposes and in certain cases produce reasonable quantitative agreement with experiments. For example, Girifalco and Weizer (1959) find that the equation of state and some elastic constants for cubic metals are accurately predicted with a Morse potential. Additionally, the current work results in predictions of phase transformation properties that compare favorably with experimental data as will be discussed in Section 5.1.

The temperature-dependent energy $\psi\begin{bmatrix} \ell \\ \alpha \end{bmatrix}(\theta)$ associated with each atom $\begin{bmatrix} \ell \\ \alpha \end{bmatrix}$ in the crystal is

$$\psi\begin{bmatrix} \ell \\ \alpha \end{bmatrix}(\theta) = \frac{1}{2} \sum_{\begin{bmatrix} \ell' \\ \alpha' \end{bmatrix} \in \Omega} \phi_{\alpha\alpha'}\left(r\begin{bmatrix} \ell & \ell' \\ \alpha & \alpha' \end{bmatrix}; \theta \right), \tag{3.1}$$

where $\phi_{\alpha\alpha'}$ is the interaction pair-potential between atoms of type α and α' and the summation runs over all atoms $\begin{bmatrix} \ell' \\ \alpha' \end{bmatrix}$ in the crystal Ω. The "self interaction energy" is assumed to be zero, i.e., $\phi_{\alpha\alpha}(0, \theta) \equiv 0$. The distance between two atoms $\begin{bmatrix} \ell \\ \alpha \end{bmatrix}$ and $\begin{bmatrix} \ell' \\ \alpha' \end{bmatrix}$ is

$$r\begin{bmatrix} \ell & \ell' \\ \alpha & \alpha' \end{bmatrix} \equiv \left\| \mathbf{x}\begin{bmatrix} \ell' \\ \alpha' \end{bmatrix} - \mathbf{x}\begin{bmatrix} \ell \\ \alpha \end{bmatrix} \right\|, \tag{3.2}$$

where $\| \cdot \|$ is the 2-norm, and the current position of each atom $\mathbf{x}\begin{bmatrix} \ell \\ \alpha \end{bmatrix}$ is given by the Lagrangian form of the CB kinematics Eq. (2.4). The internal potential energy density per unit reference volume for the crystal is calculated at a representative unit cell, $\ell = 0$,

$$\widetilde{W}(\mathbf{U}, \mathbf{S}; \theta) = \frac{1}{V} \sum_{\alpha=0}^{M-1} \psi\begin{bmatrix} 0 \\ \alpha \end{bmatrix}(\theta) = \frac{1}{2V} \sum_{\alpha=0}^{M-1} \sum_{\begin{bmatrix} \ell' \\ \alpha' \end{bmatrix} \in \Omega} \phi_{\alpha\alpha'}\left(r\begin{bmatrix} 0 & \ell' \\ \alpha & \alpha' \end{bmatrix}; \theta \right), \tag{3.3}$$

where $\mathbf{S} \equiv \{\mathbf{S}[1], \mathbf{S}[2], \ldots, \mathbf{S}[M-1]\}$ and $V = \mathbf{G}_1 \bullet (\mathbf{G}_2 \times \mathbf{G}_3)$ is the reference volume of one M-lattice unit cell. Eq. (3.3) represents the internal potential energy associated with atoms in a single unit cell located at the origin.

3.2. Stress-free equilibrium equations

The stress-free equilibrium equations involve derivatives of the energy density

$$\frac{\partial \widetilde{W}}{\partial \mathbf{U}} = \mathbf{0}, \quad \frac{\partial \widetilde{W}}{\partial \mathbf{S}[\alpha]} = \mathbf{0}, \quad \alpha = 1, 2, \ldots, M-1. \tag{3.4}$$

Eq. $(3.4)_1$ is the statement of "macroscopic" stress-free equilibrium with respect to the six components of $\mathbf{U}$. Eq. $(3.4)_2$ is the statement of inter-sub-lattice equilibrium with respect to the $3M - 3$ components of the internal shift vectors $\mathbf{S}[\alpha]$, $\alpha = 1, 2, \ldots, M - 1$. As shown in Part I, together these guarantee "microscopic" force equilibrium for each atom.

For crystals where each atom is located at a point of inversion symmetry (called a "centrosymmetric" crystal), including the $B1$, $B2$, and diamond crystal structures, force equilibrium of each atom is guaranteed under any arbitrary fixed uniform (affine) deformation $\mathbf{F}$ of the crystal (independent of the macroscopic stress generated) as noted by Born and Huang (1962) and Wallace (1998). This is the configuration for which all internal shifts $\mathbf{S}[\alpha]$ are identically zero. A point of inversion symmetry remains a point of inversion symmetry under the action of a uniform deformation (see the case of a 2-lattice in Fig. 3). It can be shown by symmetry arguments that the equilibrium Equations (3.4) for the uniform deformation DOFs and the internal shift DOFs decouple, a situation that strongly limits the types of bifurcations that can occur from centrosymmetric crystal structures. In contrast, the more general case, as in the $B19$ crystal structure, for example, can have modes of bifurcation that couple both uniform deformation and internal shifts. Furthermore, an affine deformation of a non-centrosymmetric crystal may eliminate the possibility of "microscopic" equilibrium of each atom, thereby generating fictitious "body forces" to
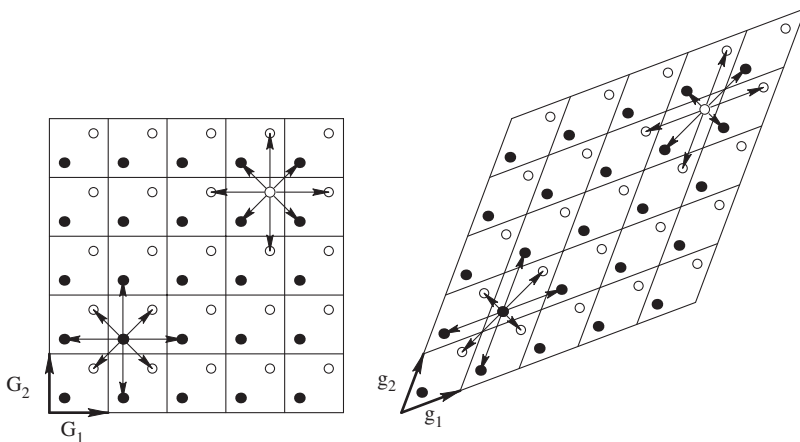

Fig. 3. A centrosymmetric 2-lattice crystal retains central inversion symmetry when subjected to any affine transformation.

obtain equilibrium. The multilattice description with its internal shifts resolves this problem and ensures equilibrium can be achieved for each atom regardless of the particular atomic potential being considered. A proof of this assertion can be found in Part I.

3.3. Stability criteria for crystalline solids

The three stability criteria for crystalline solids that were discussed in Part I are briefly outlined below (see Part I for more details).

(I) *Homogenized continuum (HC) stability*

The HC-stability criterion is the weakest criterion and indicates stability with respect to all internally equilibrated "uniform" perturbations, i.e., both the rank-one "uniform" perturbations and the "uniform" perturbations that are not rank-one (such as uniform dilation and biaxial strain). A "homogenized continuum" energy density is defined as a function only of the uniform right stretch tensor $\mathbf{U}$ by eliminating the internal shift vectors $\mathbf{S}(\mathbf{U}; \theta)$ using equilibrium Eq. $(3.4)_2$,

$$\widetilde{\widetilde{W}}(\mathbf{U}; \theta) \equiv \widetilde{W}(\mathbf{U}, \mathbf{S}(\mathbf{U}; \theta); \theta). \tag{3.5}$$

The crystal's equilibrium configuration $\overset{o}{\mathbf{U}}$ is considered HC-stable if the resulting elastic moduli (second derivative of the energy density) are positive definite with respect to all symmetric tensors $\delta\mathbf{U}$, i.e., $\widetilde{\widetilde{W}}$ is a local minimum at the equilibrium configuration[3]

$$\delta\mathbf{U} \colon \frac{\partial^2 \widetilde{\widetilde{W}}}{\partial\mathbf{U}\partial\mathbf{U}}\bigg|_{\overset{o}{\mathbf{U}}} \colon \delta\mathbf{U} > 0, \quad \forall\, \delta\mathbf{U} = \delta\mathbf{U}^{\mathrm{T}} \neq \mathbf{0}. \tag{3.6}$$

As shown in Part I, HC-stability is strictly weaker than CB-stability, and therefore, it is not used in the numerical calculations which follow.

(II) *CB-stability*

CB-stability indicates stability with respect to all quasi-uniform perturbations and contains HC-stability as a special case. Here, both the uniform right stretch tensor $\mathbf{U}$ and the internal shift vectors $\mathbf{S}[\alpha]$ are allowed to vary independently, and the crystal is considered CB-stable if $\widetilde{W}(\mathbf{U}, \mathbf{S}; \theta)$ is a local minimum, or

$$[\delta\mathbf{U}, \delta\mathbf{S}] \begin{bmatrix} \dfrac{\partial^2 \widetilde{W}}{\partial\mathbf{U}\partial\mathbf{U}} & \dfrac{\partial^2 \widetilde{W}}{\partial\mathbf{U}\partial\mathbf{S}} \\[2mm] \dfrac{\partial^2 \widetilde{W}}{\partial\mathbf{S}\partial\mathbf{U}} & \dfrac{\partial^2 \widetilde{W}}{\partial\mathbf{S}\partial\mathbf{S}} \end{bmatrix}_{\overset{o}{\mathbf{U}},\overset{o}{\mathbf{S}}} \begin{bmatrix} \delta\mathbf{U} \\[2mm] \delta\mathbf{S} \end{bmatrix} > 0,$$

$$\forall\, \delta\mathbf{U} = \delta\mathbf{U}^{\mathrm{T}} \neq \mathbf{0} \quad \text{or} \quad \delta\mathbf{S} \neq \mathbf{0}. \tag{3.7}$$

In the above equation the stability operator is of dimension $(3M + 3) \times (3M + 3)$. Here, the CB-stability criterion is defined in terms of the reference shift vector perturbations $\delta\mathbf{S}$ rather than the current shift vector perturbations $\delta\mathbf{s}$, as in Part I.

---

[3]The notation $\mathbf{A} : \mathbf{B}$ indicates double tensor right contraction defined in component form as $A_{ijkl}B_{kl}$.

These two definitions are equivalent since $\delta \mathbf{S}$ and $\delta \mathbf{s}$ are related by the (strictly) invertible relationship Eq. (2.7).

(III) *Phonon-stability*

The phonon-stability criterion considers the largest set of perturbations and indicates stability with respect to bounded perturbations of all wavelengths. It is not complete, however, since it does not investigate non-rank-one "uniform" perturbations (such as uniform dilatation and biaxial strain) or the more general quasi-uniform perturbations, which are addressed by CB-stability. In the phonon-stability calculations equilibrium configurations conform to CB kinematics (quasi-uniform deformation) but stability is evaluated with respect to all bounded perturbations. All atoms in the crystal are given their three translational degrees of freedom and the linearized equations of motion are considered. Taking advantage of the translational symmetry of the multilattice the corresponding stiffness matrix is block-diagonalized by a block-Fourier transform resulting in the *dynamical matrix* $\mathbb{K}^j{}_k \left[{\mathbf{k} \atop \alpha\ \alpha'} \right]$, a $3M \times 3M$ matrix (where M is the number of atoms in the unit cell) for each wave vector $\mathbf{k}$, given by

$$\mathbb{K}^j{}_k \left[{\mathbf{k} \atop \alpha\ \alpha'} \right] = (m_\alpha m_{\alpha'})^{-1/2} \sum_{\ell' \in \mathbb{Z}^3} G^{jp} \overset{o}{\varPhi}_{pk} \left[{0\ \ \ell' \atop \alpha\ \ \alpha'} \right] \exp\left\{ -i\mathbf{k} \bullet \left(\mathbf{X}\left[{\ell' \atop \alpha'} \right] - \mathbf{X}\left[{0 \atop \alpha} \right] \right) \right\},$$
(3.8)

where m_α is the mass of atom α, $\mathbb{Z}^3$ is the set of all lattice points in the infinite crystal, and $\overset{o}{\varPhi}_{pk} \left[{\ell\ \ell' \atop \alpha\ \alpha'} \right]$ is the stiffness coefficient between atoms $\left[{\ell \atop \alpha} \right]$ and $\left[{\ell' \atop \alpha'} \right]$. The wave vector $\mathbf{k}$ ranges over values in the unit cell of the reciprocal reference lattice (multiplied by a factor of 2π)

$$\mathbf{k} \in \{k_i \mathbf{G}^i \mid -\pi \leqslant k_i < \pi\}.$$
(3.9)

The eigenvalues of the dynamical matrix are real (due to the Hermitian nature of $\mathbb{K}$) and satisfy the relation

$$(\omega^{(q)}(\mathbf{k}))^2 \Delta\widehat{v}^j \left[{\mathbf{k} \atop \alpha} \right]^{(q)} = \sum_{\alpha'=0}^{M-1} \mathbb{K}^j{}_p \left[{\mathbf{k} \atop \alpha\ \alpha'} \right] \Delta\widehat{v}^p \left[{\mathbf{k} \atop \alpha'} \right]^{(q)}.$$
(3.10)

The squared phonon frequencies $(\omega^{(q)}(\mathbf{k}))^2$ must all be positive for the crystal to be stable[4], i.e.,

$$(\omega^{(q)}(\mathbf{k}))^2 > 0 \begin{cases} \text{for } \mathbf{k} \neq \mathbf{0}, & q = 1, 2, \ldots, 3M; \\ \text{for } \mathbf{k} = \mathbf{0}, & q = 4, 5, \ldots, 3M. \end{cases}$$
(3.11)

For "material stability" under soft-device loading conditions, as defined in Part I, the CB-stability criterion and the phonon-stability criterion must be satisfied. This ensures stability with respect to all quasi-uniform perturbations (CB) and bounded displacement perturbations of all wavelengths (phonon).

---

[4]The acoustic phonons at $\mathbf{k} = \mathbf{0}$ and $q = 1, 2, 3$ have been excluded since their frequencies are identically zero and correspond to the rigid-body translation modes of the crystal.

3.4. Parameters and solution procedures

At this point we are interested in finding all connected equilibrium paths which are solutions to the set of non-linear algebraic equations (3.4) associated with a particular choice of DOFs (fixed M-lattice). Thus, CB-stability identifies critical points, and asymptotic analyses help to enumerate bifurcated paths. In this section, the particular atomic potentials used in the remainder of this paper are specified. Next, numerical methods for finding connected equilibrium paths and critical points are discussed. Finally, details of the numerical evaluation of the stability criteria of Section 3.3 are presented.

3.4.1. Temperature-dependent Morse pair-potentials

The case of temperature-dependent interatomic forces is investigated by Sutton (1989) where he takes advantage of the anharmonicity (asymmetry) of 0 K atomic interactions to derive temperature-dependent potentials from a knowledge of the phonon frequencies of the crystal. Others follow a similar approach, including Melker and Ivanov (2000) who introduce temperature-dependent Morse pair-potentials for hydrogen-hydrogen, carbon–carbon, and hydrogen–carbon interactions in polymers, and Zarkova (1996) who introduced a set of Lennard–Jones pair-potentials with temperature-dependent parameters. In this last case, a statistical mechanics approach based on excited quantum states of the particles is used to derive temperature-dependent binding-energy and equilibrium separation coefficients. The work by Brown et al. (1997) is also interesting, where an empirical valence conservation principle is used to derive the bond length and bond force constant as a function of temperature for each bond in a set of 12 different inorganic compounds.

The material model to be used here is based on central-force Morse pair-potentials that are temperature-dependent. In Elliott et al. (2002a, b) the atomic bond stiffness of the Morse potential was made temperature-dependent. Here, instead, it is assumed that the natural pair equilibrium separation $\hat{r}(\theta)$ is temperature-dependent as

$$\hat{r}(\theta) = r_0 + r_\theta(\theta - 1), \tag{3.12}$$

where r_0 is the constant reference equilibrium separation, $\theta \equiv T/T_0$ is a dimensionless absolute temperature, T_0 is the reference temperature taken to be 300 K (typical room temperature), and r_θ is a constant related to the thermal expansion of the natural atomic bond length. In this way, the energy of each atomic bond type in the crystal can be expressed as[5]

$$\phi(r; \theta) \equiv A\left\{\exp\left[-2B\left(\frac{r}{\hat{r}(\theta)} - 1\right)\right] - 2\exp\left[-B\left(\frac{r}{\hat{r}(\theta)} - 1\right)\right]\right\}, \tag{3.13}$$

where A and B are constants associated with binding energy and bond stiffness, respectively.

The Morse pair-potential is chosen for its exponential form, which rapidly decays to zero with increasing r. For computational purposes, the summation over all atoms in Eq. (3.3) is truncated at the boundary of an "Eulerian sphere of influence". The radius of this sphere is chosen such that the total energy contribution associated with atoms outside

---

[5]Subscripts indicating the types of atoms involved in the interaction are suppressed to avoid cumbersome notation.
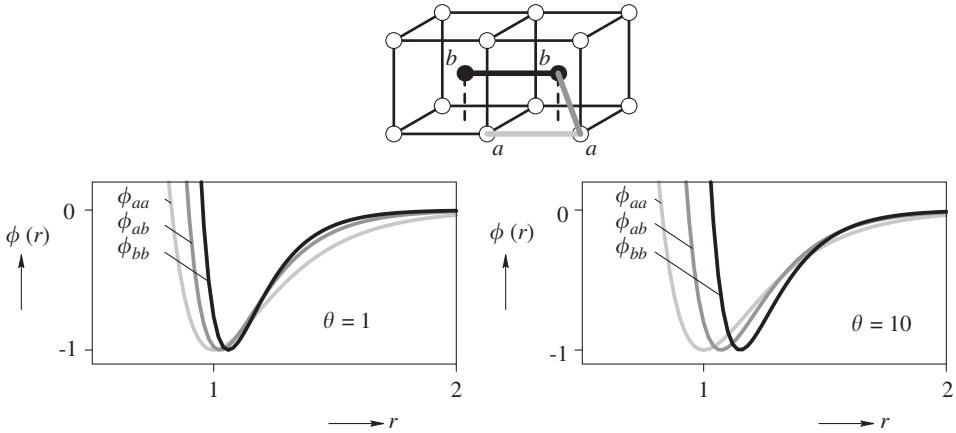
Fig. 4. Three temperature-dependent pair-potentials for the $B2$ crystal structure at $\theta = 1$ and 10 (an exaggerated temperature, chosen for clarity).

Table 1
Pair-potential parameters used in numerical calculations

Bond	r_0	r_θ	A	B
aa	1	0	1	4
bb	1.060347	0.010	1	7
ab	1.026362	0.005	1	5.5

the sphere is negligible.[6] It is found that the Morse pair-potentials used here require an influence radius no larger than seven reference lattice spacings to achieve convergence of the summations in the energy density Eq. (3.3) and of all of its derivatives.

The popular alloy NiTi is chosen as a prototypical SMA. Its austenite phase is the $B2$ cubic crystal structure for which there are three different types of atomic interactions, two like-interactions aa and bb and unlike-interaction ab (see Fig. 4). The numerical values of the bond parameters used in the numerical calculations that follow are given in Table 1.

Dimensionless potentials are created by normalizing parameters with respect to the aa interaction. The parameters for the like-bonds are chosen to reasonably match elastic moduli of pure Ni (aa) and pure Ti (bb) individually, although it is not possible to match all the elastic moduli due to the Cauchy relations arising from the central-force pair-potentials. This procedure determines the values of B^{aa} and B^{bb}, and then B^{ab} is set to their average. A variety of values were investigated for the remaining parameters. The aa bond is taken to be temperature-independent, $r_\theta^{aa} = 0$, and the thermal expansion coefficient of

---

[6]A cautionary word to those trained in continuum mechanics. One must resist the temptation to use a Lagrangian sphere of influence and simply sum interactions over a fixed set of atoms in the reference configuration. Finite deformation of the crystal can cause an incomplete and distorted summation of atomic interactions in the current configuration. This leads to numerically introduced imperfections that mask bifurcation points and leads to incorrect interpretations of crystal symmetries.

NiTi is matched to within a factor of two by the choice of r_θ^{bb}. The reference equilibrium separation r_0^{bb} is chosen so that the critical point on the $B2$ equilibrium path occurs near $\theta = 1$, and r_0^{ab} is chosen such that interesting stability behavior occurs. The model is quite sensitive to the relative values of r_0^{bb} and r_0^{ab}, so these are reported to seven significant digits in Table 1. The three bond energies at two different dimensionless temperatures θ are shown in Fig. 4.

3.4.2. Calculation of stress-free equilibrium paths

Once an equilibrium path has been identified (either through inspection of the equilibrium Eqs. (3.4), an asymptotic analysis about a bifurcation point, or a numerical search), the associated crystal structure is determined, and a minimal set of DOFs is identified to describe the equilibrium path. For example, due to the centrosymmetric nature of the $B2$ crystal structure, it follows that a stress-free equilibrium path exists for uniform thermal expansion (principal branch). This is a cubic crystal structure that requires only a single DOF, the lattice parameter, $a(\theta)$,

$$\mathbf{U}(\theta)_{\text{cubic}} = a(\theta)\mathbf{I}; \quad \mathbf{S}[\alpha](\theta) = \mathbf{0}, \quad \forall \alpha. \tag{3.14}$$

In general there are m DOFs ($m \leqslant 3M + 3$), and once identified, the corresponding subset of nonlinear algebraic equations (3.4) is solved using an incremental Newton–Raphson scheme. It is convenient to introduce the DOF vector $\mathbf{u} \in \mathbb{R}^{(3M+3)}$ defined by

$$\mathbf{u} \equiv \{\mathbf{U}, \mathbf{S}\}. \tag{3.15}$$

Riks (1979) method (arc-length following algorithm) and the Newton–Raphson scheme are used to find points along an equilibrium path and facilitate the crossing of limit-loads that may be encountered (see Elliott et al., 2002b, for further details). The requirement that a new solution be found at a specified "distance", Δd, from the most recently found equilibrium solution, i.e.,

$$\|\Delta\mathbf{u}\|^2 + (\Delta\theta)^2 = (\Delta d)^2, \tag{3.16}$$

is used to augment the equilibrium equations (3.4).

From the CB-stability criterion critical points are found by detecting zero eigenvalues of the stability operator $\partial^2 \widetilde{W} / \partial\mathbf{u}^2$. The eigen-modes $\overset{(I)}{\mathbf{u}}$ corresponding to zero eigenvalues of the stability operator are found from

$$\left.\frac{\partial^2 \widetilde{W}}{\partial\mathbf{u}\partial\mathbf{u}}\right|_c \bullet \overset{(I)}{\mathbf{u}} = \mathbf{0}, \quad I = 1, 2, \ldots, H; \tag{3.17}$$

where the subscript c indicates evaluation of the derivative at the critical point $(\mathbf{u}_c, \theta_c)$, θ_c is the critical temperature, $\mathbf{u}_c = \overset{o}{\mathbf{u}}(\theta_c)$, and H is the multiplicity of the critical point. The type of critical point (limit-load or bifurcation point) is identified by the following test (see Triantafyllidis and Peek, 1992):

$$\left.\frac{\partial^2 \widetilde{W}}{\partial\mathbf{u}\partial\theta}\right|_c \bullet \overset{(I)}{\mathbf{u}} \begin{cases} \neq 0 & \text{limit-load point,} \\ = 0 & \text{bifurcation point.} \end{cases} \tag{3.18}$$

When a bifurcation point is detected two procedures are invoked. First, a bi-section method (on Δd) is used to accurately determine the critical temperature and kinematic

DOFs. Secondly, a Lyapunov–Schmidt–Koiter (LSK) decomposition is performed and the bifurcation equations are determined. These equations are summarized here, but the reader is referred to the discussions in Elliott et al. (2002b) and Triantafyllidis and Peek (1992) for further details. At the bifurcation point each equilibrium path is parameterized by its bifurcation amplitude parameter ξ. The path's deformation vector $\mathbf{u}$ and the temperature θ are expanded in powers of ξ as

$$\mathbf{u}(\xi) = \overset{o}{\mathbf{u}}(\theta(\xi)) + \xi \sum_{I=1}^{H} \alpha_I \overset{(I)}{\mathbf{u}} + \frac{\xi^2}{2} \sum_{I,J=1}^{H} \alpha_I \alpha_J \overset{(IJ)}{\mathbf{V}} + O(\xi^3),$$

$$\theta(\xi) = \theta_c + \xi\theta_1 + \frac{\xi^2}{2}\theta_2 + O(\xi^3), \quad \|\boldsymbol{\alpha}\| = 1, \tag{3.19}$$

where quantities $\overset{(IJ)}{\mathbf{V}}$ satisfy

$$\left.\begin{aligned}
\left.\frac{\partial^2 \widetilde{W}}{\partial\mathbf{u}\partial\mathbf{u}}\right|_c \bullet \overset{(IJ)}{\mathbf{V}} &= -\left(\left.\frac{\partial^3 \widetilde{W}}{\partial\mathbf{u}\,\partial\mathbf{u}\,\partial\mathbf{u}}\right|_c \bullet \overset{(I)}{\mathbf{u}}\right) \bullet \overset{(J)}{\mathbf{u}}, \\
\overset{(IJ)}{\mathbf{V}} \bullet \overset{(K)}{\mathbf{u}} &= 0,
\end{aligned}\right\} \quad I,J,K = 1,2,\ldots,H; \tag{3.20}$$

$\overset{o}{\mathbf{u}}(\theta)$ describes the principal equilibrium path on which the bifurcation point is encountered, and any convenient norm on $\boldsymbol{\alpha}$, the tangent[7] of the bifurcated path at θ_c, may be employed. The lowest-order terms in the asymptotic development are found by corresponding lowest-order expansion of the equilibrium equations in the null-space of the stability operator, resulting in

$$\text{If } \theta_1 \neq 0: \sum_{J,K=1}^{H} \alpha_J \alpha_K \mathscr{E}_{IJK} + 2\theta_1 \sum_{J=1}^{H} \alpha_J \mathscr{E}_{IJ\theta} = 0; \quad I = 1,2,\ldots,H;$$

or

$$\text{If } \theta_1 = 0: \sum_{J,K,L=1}^{H} \alpha_J \alpha_K \alpha_L \mathscr{E}_{IJKL} + 3\theta_2 \sum_{J=1}^{H} \alpha_J \mathscr{E}_{IJ\theta} = 0; \quad I = 1,2,\ldots,H. \tag{3.21}$$

If the coefficients $\mathscr{E}_{IJK}$ (defined below) are all zero then $\theta_1 = 0$ and solutions to Eq. (3.21)$_2$ are used; otherwise, solutions to Eq. (3.21)$_1$ are determined. The coefficients $\mathscr{E}_{IJK}$, $\mathscr{E}_{IJKL}$, and $\mathscr{E}_{IJ\theta}$ $(I,J,K,L = 1,\ldots,H)$ are related to higher-order derivatives of the energy density $\widetilde{W}$ and are defined by

$$\mathscr{E}_{IJK} \equiv \left[\frac{\partial^3 \widetilde{W}}{\partial u_i \,\partial u_j \,\partial u_k}\right]_c \overset{(I)}{u_i} \overset{(J)}{u_j} \overset{(K)}{u_k},$$

---

[7]Note that when the bifurcation amplitude parameter ξ is eliminated, the equilibrium path's displacements $\mathbf{u}(\theta)$ may be quadratic in the nondimensionalized temperature $\Delta\theta$ and the α_I then actually represent curvatures.

$$\mathcal{E}_{IJKL} \equiv \left[\frac{\partial^4 \widetilde{W}}{\partial u_i \, \partial u_j \, \partial u_k \, \partial u_l} \right]_c \overset{(I)}{u}_i \overset{(J)}{u}_j \overset{(K)}{u}_k \overset{(L)}{u}_l$$

$$+ \left[\frac{\partial^3 \widetilde{W}}{\partial u_i \, \partial u_j \, \partial u_k} \right]_c \left(\overset{(J)}{u}_j \overset{(KL)}{V}_k + \overset{(K)}{u}_j \overset{(JL)}{V}_k + \overset{(L)}{u}_j \overset{(JK)}{V}_k \right) \overset{(I)}{u}_i,$$

$$\mathcal{E}_{IJ\theta} \equiv \left[\frac{d}{d\theta} \left(\frac{\partial^2 \widetilde{W}(\overset{o}{\mathbf{u}}(\theta);\theta)}{\partial u_i \partial u_j} \right) \right]_c \overset{(I)}{u}_i \overset{(J)}{u}_j. \tag{3.22}$$

Practically, Eqs. (3.22) are evaluated numerically and Eq. (3.21) can be solved by inspection. A "transcritical" (or "asymmetric") bifurcation occurs when $\theta_1 \neq 0$. The system of H quadratic equilibrium Eqs. $(3.21)_1$ for α_I has at most $2^H - 1$ nontrivial independent real solutions, each corresponding to an equilibrium path. When $\theta_1 = 0$, a "symmetric" bifurcation occurs, and Eq. $(3.21)_2$ determines the tangents α_I. There are at most $(3^H - 1)/2$ nontrivial pairs of real solutions $(+\alpha_I, -\alpha_I)$. Each pair of solutions corresponds to one equilibrium path. The coefficients Eqs. (3.22) and the quantities $\overset{(IJ)}{\mathbf{V}}$ are evaluated numerically and the bifurcation Eqs. (3.21) are solved, providing an initial solution on the new bifurcation branch that can then be followed by the arc-length procedure.

The stability (CB-stability) in the neighborhood of the bifurcation point of emerging equilibrium paths is governed, according to the general theory by Triantafyllidis and Peek (1992), by the signs of the eigenvalues of the matrix **B**, defined by

$$\text{If } \theta_1 \neq 0: \quad B_{IJ}(\boldsymbol{\alpha}) \equiv \theta_1 \mathcal{E}_{IJ\theta} + \sum_{K=1}^{H} \alpha_K \mathcal{E}_{IJK},$$

or

$$\text{If } \theta_1 = 0: \quad B_{IJ}(\boldsymbol{\alpha}) \equiv \theta_2 \mathcal{E}_{IJ\theta} + \sum_{K,L=1}^{H} \alpha_K \alpha_L \mathcal{E}_{IJKL}. \tag{3.23}$$

A transverse bifurcation path has stability matrix given by Eq. $(3.23)_1$ and is CB-unstable in the neighborhood of the bifurcation point if the matrix **B** has eigenvalues of both signs. If all eigenvalues have the same sign, then the path has a change of CB-stability as the critical point is crossed. A symmetric bifurcation path has stability matrix given by Eq. $(3.23)_2$ and is CB-stable near the bifurcation point if **B** is positive definite and CB-unstable otherwise.

3.4.3. Numerical stability calculations

The stability of general CB equilibrium configurations is evaluated numerically by the CB-stability and phonon-stability criteria as follows:

(I) The CB-stability criterion is evaluated directly from the second derivative of the energy density $\widetilde{W}(\mathbf{U}, \mathbf{S}; \theta)$ and the eigenvalues are found using the cyclic Jacobi method (Patel, 1994) for symmetric matrices.

(II) The procedure to evaluate phonon-stability is more complicated. The coefficients $\overset{o}{\Phi}_{jk}\begin{bmatrix} \ell & \ell' \\ \alpha & \alpha' \end{bmatrix}$ are given explicitly in terms of derivatives of the temperature-dependent

pair-potentials as

$$
\overset{o}{\Phi}_{jk}\begin{bmatrix} \ell & \ell' \\ \alpha & \alpha' \end{bmatrix} = \begin{cases} -2\varphi'_{\alpha,\alpha'} G_{jk} - 4\varphi''_{\alpha,\alpha'} \left(x_j\begin{bmatrix} \ell \\ \alpha \end{bmatrix} - x_j\begin{bmatrix} \ell' \\ \alpha' \end{bmatrix} \right) & \ell \neq \ell', \\ \qquad\qquad \times \left(x_k\begin{bmatrix} \ell \\ \alpha \end{bmatrix} - x_k\begin{bmatrix} \ell' \\ \alpha' \end{bmatrix} \right), & \\ -\sum_{\ell'' \neq \ell'} \overset{o}{\Phi}_{jk}\begin{bmatrix} \ell & \ell'' \\ \alpha & \alpha' \end{bmatrix}, & \ell = \ell', \end{cases}
$$
(3.24)

where $\varphi(r^2; \theta) \equiv \phi(r; \theta)$, and φ' and φ'' are the respective first and second derivatives with respect to r^2 of the atomic pair-potentials Eq. (3.13). Additionally, the components of the dynamical matrix, Eq. (3.8), with respect to a Cartesian coordinate system are

$$
\mathbb{K}_{jk}\begin{bmatrix} \mathbf{k} \\ \alpha\ \alpha' \end{bmatrix} = A_{jm} A_k^n \mathbb{K}_n^m\begin{bmatrix} \mathbf{k} \\ \alpha\ \alpha' \end{bmatrix},
$$
(3.25)

where the A matrices, given by

$$
A_{jm} \equiv \mathbf{e}_j \bullet \mathbf{G}_m, \quad A_k^n \equiv \mathbf{e}_k \bullet \mathbf{G}^n,
$$
(3.26)

transform the spatial coordinate components ($\mathbb{K}_n^m\begin{bmatrix} \mathbf{k} \\ \alpha\ \alpha' \end{bmatrix}$) to the orthonormal Cartesian system $\mathbf{e}_i$ ($\mathbb{K}_{jk}\begin{bmatrix} \mathbf{k} \\ \alpha\ \alpha' \end{bmatrix}$). Thus, $\mathbb{K}_{jk}\begin{bmatrix} \mathbf{k} \\ \alpha\ \alpha' \end{bmatrix}$ are the components of a Hermitian matrix. The dimensionless atomic masses (normalized with respect to Ni) for Ni (a) and Ti (b) are $m_a = 1$ and $m_b = 0.816$. The dynamical matrix, Eq. (3.25), is calculated for any given wave vector $\mathbf{k}$ and its eigenvalues are found using the cyclic Jacobi method, modified for complex Hermitian matrices. Theoretically, stability must be evaluated for a continuum of wave vectors lying within a single reciprocal lattice unit cell. Practically, however, a discrete grid of values (size $22 \times 22 \times 22$) gives robust results, since sufficient continuity of the dynamical matrix with respect to $\mathbf{k}$ components exists. As was shown in Part I, the phonon frequencies for $\mathbf{k}$ and $-\mathbf{k}$ are equal. Therefore, only one half of the reciprocal unit cell is investigated ($22 \times 22 \times 12$ grid). Depending on the point symmetry of the deformed crystal, a region smaller than half of the unit cell may be enough to investigate all unique phonon frequencies. Indeed, for equilibrium configurations with cubic symmetry, only 1/48th of the unit cell needs to be considered. However, calculations are performed across one entire half of the reciprocal unit cell to accommodate crystals of any point group symmetry.

4. Numerical results for a 2-lattice

In this section the bifurcation and stability properties of the cubic $B2$ crystal structure (space symmetry group $Pm3m$, see further US NRL Center for Computational Materials Science, 2004) are investigated. The $B2$ crystal structure can be described using a primitive unit cell that contains two different atoms, and therefore a 2-lattice description is appropriate. Although the choice of M-lattice description for the crystal does not affect the stability results for an equilibrium configuration, it does restrict the set of equilibrium configurations that can be found. In the course of an equilibrium path stability investigation, the phonon-stability criterion may identify a bifurcating equilibrium path

that is unobtainable with the 2-lattice proposed here. In this case an *M*-lattice with more DOFs must be adopted to investigate the new equilibrium path. This is exactly what happens in the current model and, as discussed in Section 4.3, a 4-lattice model will ultimately be needed.

The reference fractional position vectors for the atoms are given by

$$\mathbf{P}[\alpha] \equiv \begin{cases} 0, & \alpha = 0, \\ \frac{1}{2}\,\mathbf{G}_1 + \frac{1}{2}\,\mathbf{G}_2 + \frac{1}{2}\,\mathbf{G}_3, & \alpha = 1, \end{cases} \tag{4.1}$$

where $\mathbf{G}_i \equiv a\mathbf{e}_i$ are the simple cubic reference lattice vectors of length a (see Eq. (3.14) and Fig. 2) and $\mathbf{e}_i$ are a set of orthonormal vectors aligned with the cubic axes. As indicated in Fig. 2, $\mathbf{S}[0]$ is set to zero to eliminate rigid-body translation modes.

4.1. Stress-free equilibrium paths—CB-stability

The above 2-lattice description and the temperature-dependent atomic pair-potentials of Section 3.4.1 are used to construct a thermo-elastic energy density $\widetilde{W}(\mathbf{U}, \mathbf{S}; \theta)$. The numerical methods of Section 3.4.2 are used to solve the stress-free equilibrium Eqs. (3.4) to determine all equilibrium paths that are connected (either directly or through an intermediate path) to the *B*2 crystal's thermal expansion path. This results in the bifurcation diagram of Fig. 5 which shows the U_{33} component of the right stretch tensor (with respect to the orthonormal basis $\mathbf{e}_i$ aligned with the cubic axes) as a function of dimensionless temperature θ, and the dimensionless energy density $\widetilde{W}/\mu$ as a function of temperature, where μ is the reference equilibrium shear modulus of the material given by

$$\mu \equiv \left. \frac{\partial^2 \widetilde{W}}{\partial U_{12} \partial U_{12}} \right|_{(\mathbf{U}=\mathbf{I},\, \mathbf{S}=\mathbf{0};\, \theta=1)}. \tag{4.2}$$

In Fig. 5(a) the *B*2 crystal is shown to be CB-stable (indicated by the solid line) at high temperatures. At the bifurcation point $\mathscr{A}$ (open circle) where $\theta = 0.66$ the *B*2 crystal becomes unstable (dashed line) and remains unstable for lower temperatures. Point $\mathscr{A}$ is a multiple bifurcation point and an LSK analysis (see Elliott, 2004) determines that three variants of the tetragonal $L1_0$ (space group *P4/mmm*) crystal structure emerge from this critical point, only one of which is shown in Fig. 5. The remaining two variants can be obtained from symmetry considerations. See Appendix A for a more complete description of the $L1_0$ crystal structure. The $L1_0$ crystal corresponds to an affine deformation of the *B*2 crystal structure and accordingly has all of its internal shifts equal to zero (i.e., $\mathbf{S} = \mathbf{0}$). The LSK results predict that the $L1_0$ path crosses the *B*2 path transversely ($\theta_1 \neq 0$) and is initially CB-unstable. A comparison between the asymptotic expression (dotted line) for U_{33} (Elliott, 2004) and the numerically determined states (filled squares) for the $L1_0$ crystal structure is shown in Fig. 6. The excellent agreement between the analytical and numerical results provides a useful check on the numerical calculations.

Following the bifurcated $L1_0$ equilibrium branch upward from point $\mathscr{A}$ in Fig. 5(a) the $L1_0$ path eventually reaches a limit-load in temperature near $\theta = 4.43$ (filled circle), after which it is CB-stable for the remaining segment of the path. The dimensionless energy densities of the *B*2 and $L1_0$ equilibrium paths are plotted as a function of temperature in
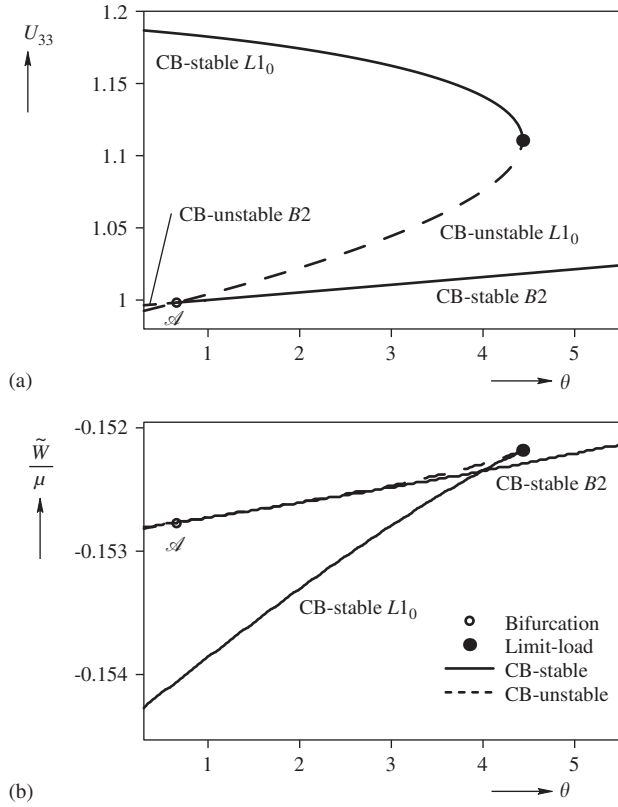
Fig. 5. Calculated 2-lattice stress-free equilibrium bifurcation and CB-stability diagrams showing: (a) U_{33} component of the deformation and (b) dimensionless energy density $\widetilde{W}/\mu$ versus dimensionless temperature θ.
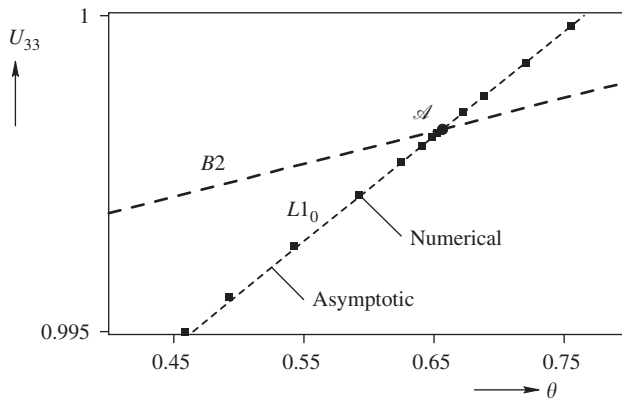

Fig. 6. Asymptotic verification of bifurcated $L1_0$ tetragonal equilibrium path.

Fig. 5(b). The higher symmetry $B2$ cubic phase and the lower symmetry $L1_0$ tetragonal phase have CB-stable overlapping segments in temperature, and thus, the possibility of a proper martensitic phase transformation is indicated. At sufficiently high temperatures, the

$B2$ crystal structure is the only stable phase. At intermediate temperatures both the $B2$ and the $L1_0$ crystal structures are stable but below $\theta = 3.98$ the $L1_0$ branch has lower energy. For temperatures below $\theta = 0.66$ the $L1_0$ structure is the only stable phase. The overlap in stable segments between the two phases at the critical point $\mathscr{A}$ and the limit-load near $\theta = 4.43$ indicate that temperature-induced transformations would be hysteretic. It is worth mentioning at this point that these two crystal structures are, in fact, the austenite and martensite phases found in the SMA NiAl (see, for example Shao et al., 1996). However, the final determination of stability for the $B2$ and $L1_0$ branches requires consideration of phonon-stability, which is included in the next section.

4.2. Stress-free equilibrium paths—phonon-stability

While the above results appear promising, they are not the final conclusion regarding stability. Fig. 7 shows the same set as in Fig. 5(a) of stress-free equilibrium paths for the 2-lattice description but with stability now evaluated by the phonon-stability criterion. Comparing Fig. 7 with 5(a) shows that the two stability criteria produce different results. The phonon-stability criterion predicts a higher critical temperature (point $\mathscr{B}$, $\theta = 0.97$) of the $B2$ phase compared to the CB-stability criterion (point $\mathscr{A}$, $\theta = 0.66$). The $L1_0$ tetragonal path emerges from $\mathscr{A}$ and is initially phonon-unstable, in agreement with the CB-stability criterion, but now it remains phonon-unstable as it crosses the limit-load near $\theta = 4.43$. This is in contrast to the CB-stability results and leaves the $B2$ crystal as the only phonon-stable crystal in the entire 2-lattice bifurcation diagram. The difference between the CB-stability and phonon-stability results illustrates the importance of investigating bounded perturbations of all wavelengths. Indeed, if the CB-stability criterion is considered alone, a proper martensitic transformation between the $B2$ and $L1_0$ crystal structures would be expected to occur, but the phonon-stability results clearly show that no such transformation would occur.

The differences between CB- and phonon-stability are highlighted by examining the phonon frequencies along the thermal expansion (principal) path of the $B2$ crystal
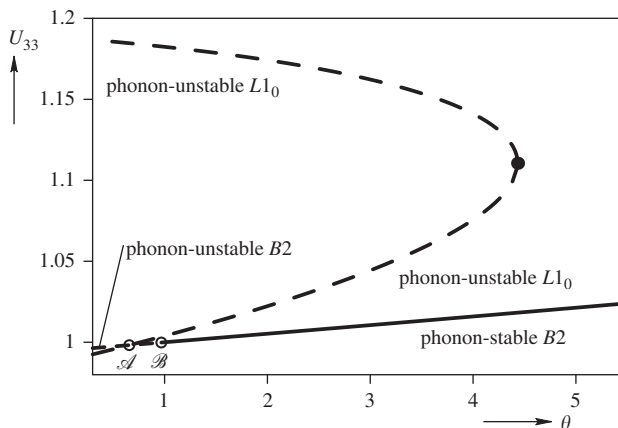

Fig. 7. Calculated 2-lattice stress-free equilibrium bifurcation and phonon-stability diagram showing the U_{33} component of deformation.
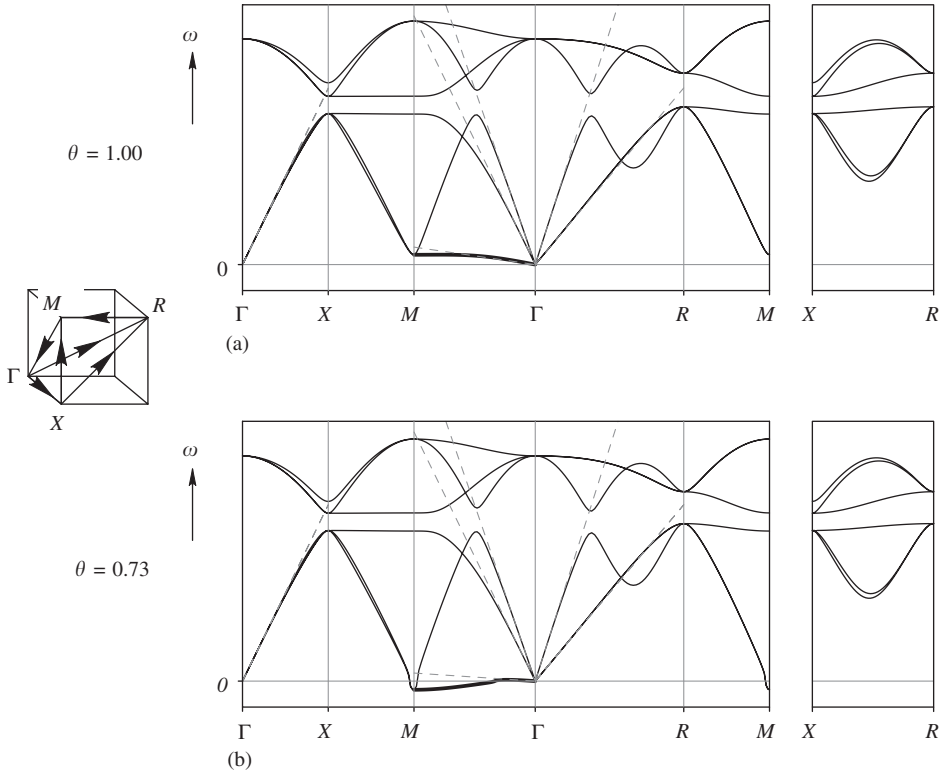
Fig. 8. Dispersion curves for the $B2$ crystal along high symmetry directions (solid lines) and long wavelength asymptotic results (dashed lines) at two temperatures.

structure. Although the entire space of **k** values is investigated numerically, Fig. 8 shows a conventional plot of phonon frequencies (Dove, 1993), the square-root of the eigenvalues of Eq. (3.25), at two different temperatures for a specific set of wave vectors **k**. The diagram on the left in Fig. 8 depicts selected sets of wave vectors within the first octant $(0 \leqslant k_i \leqslant \pi)$ of the reciprocal lattice unit cell. The point Γ is the origin and is located at the body center of the reciprocal unit cell, X is located at the center of the unit cell's face, M is a unit cell edge midpoint, and R is a unit cell corner. These sets of wave vectors correspond to phonon modes oriented along high symmetry directions in the real cubic crystal, and the associated cyclic phonon frequencies are plotted in Fig. 8.

The $B2$ phonon dispersion curves for the reference temperature $\theta = 1.0$ are displayed in Fig. 8(a). Note that there are six different branches in this figure corresponding to the three acoustic branches attached at the origin Γ and the $(3M - 3) = 3$ optic branches (for the current case of $M = 2$). For simplicity, real phonon frequencies are plotted as positive; whereas, purely imaginary frequencies are plotted as negative. All of the phonon modes shown at the reference temperature $\theta = 1$ are stable. Fig. 8(b) shows the dispersion curves for the $B2$ crystal structure at the lower temperature of $\theta = 0.73$ (between $\mathscr{A}$ and $\mathscr{B}$ in Fig. 7) where the CB- and phonon-stability results disagree. Unstable phonon modes now exist between M and Γ. Segments of the dispersion curves near point Γ (**k** = **0**) correspond

to long wavelength phonons; whereas, segments near the other points (X, M, and R) correspond to short wavelength phonon modes. Note that all long wavelength modes near Γ are stable, yet some short wavelength modes near M are unstable. This illustrates the nature of the discrepancy between the phonon- and CB-stability criteria. The former investigates bounded perturbations of all wavelengths; whereas, the latter considers only quasi-uniform perturbations. Therefore, CB-stability is unable to detect the short wavelength mode that causes the instability at $\mathscr{B}$.

At point $\mathscr{B}$ ($\theta = 0.97$), two of the phonon frequency branches at M (short wavelength modes) become zero, called "soft phonon modes" (Dove, 1993), indicating the first instability upon cooling and the presence of a bifurcation point along the $B2$ path. As the temperature decreases from $\mathscr{B}$ towards $\mathscr{A}$ these dispersion branches near M in Fig. 8 continue to descend and longer wavelength phonons also become unstable. Thus, a finite wavelength phonon mode exists with zero frequency for each temperature between $\mathscr{B}$ and $\mathscr{A}$. The phonon modes with irrational wavelength, known as "incommensurate" modes (Dove, 1993) where the wavelength of the perturbation is unrelated to the periodicity of the crystal, give rise to "incommensurate bifurcated equilibrium paths" that require an infinite number of DOFs for their description. In contrast, the "commensurate" (or periodic) phonon modes give rise to "commensurate bifurcated equilibrium paths" that require a finite number of DOFs for their description.

The straight dashed lines connected to point Γ in Fig. 8 are the dispersion relations for the homogenized elastic waves of the HC model discussed in Part I. The slopes of these lines are determined by the natural frequencies of the mass normalized acoustic tensor $\mathbf{A}(\mathbf{k})$ given by

$$A_{ij}(\mathbf{k}) \equiv \frac{1}{\rho} \left. \frac{\partial^2 \overset{\approx}{W}}{\partial F^i{}_m \partial F^j{}_n} \right|_{\overset{o}{\mathbf{u}}} k_m k_n, \qquad (4.3)$$

where ρ is the reference mass density of the crystal. The elastic waves correspond to the long wavelength acoustic phonon modes ($\mathbf{k} \to \mathbf{0}$) as proved in Part I. These asymptotic results are accurate across a considerable interval near the origin Γ. In other words, the crystal behaves as a continuum under both moderate and long wavelength perturbations. Additionally, the agreement between these two different calculations serves as a verification of the numerical results.

It is interesting to compare the dispersion curves of Fig. 8 to those of Huang et al. (2002) which are reproduced in Fig. 9, where a plane-wave pseudopotential variation of density-functional theory is used to calculate the dispersion curves for $B2$ NiTi at 0 K. There is considerable qualitative agreement between the current pair-potential calculations and the more sophisticated calculations of Huang et al. (2002). Both results show instability at M and similar shapes to the curves, which likely arises from the cubic symmetry of the $B2$ crystal.

4.3. Critical deformation modes at $\mathscr{B}$

The phonon-stability criterion identifies an infinite number of bifurcation points ($\omega(\mathbf{k}) = 0$) for temperatures below $\mathscr{B}$ ($\theta = 0.97$), some of which could potentially have bifurcating equilibrium paths with stable segments. Only the $L1_0$ tetragonal bifurcation point $\mathscr{A}$ is accessible to the 2-lattice description of the $B2$ crystal and therefore a new
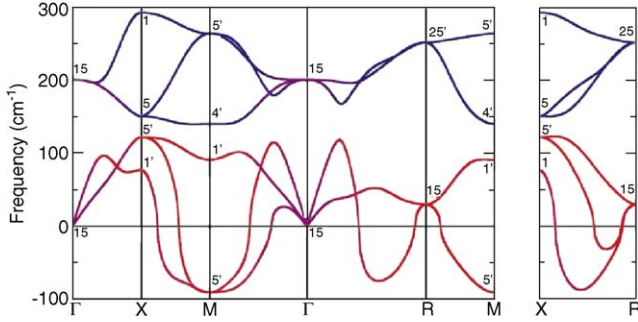
Fig. 9. Dispersion curves for the $B2$ cubic crystal structure of NiTi at 0 K. (Reprinted figure with permission from Huang et al., Physical Review B–Condensed Matter, 65, 014108/1–5, 2002. Copyright (2002) American Physical Society.)

description is needed with more atoms per unit cell to investigate other bifurcation points (including $\mathscr{B}$). It is a daunting, if not impossible, task to consider the continuum of points between $\mathscr{A}$ and $\mathscr{B}$, but it seems reasonable to study point $\mathscr{B}$ since it represents the onset of instability upon cooling along the principal branch. The three reciprocal cell-edge midpoints (symmetry related points M) correspond to wave vectors of

$$\mathbf{k}_{M1} = \pi\mathbf{G}^1 + \pi\mathbf{G}^2, \quad \mathbf{k}_{M2} = \pi\mathbf{G}^2 + \pi\mathbf{G}^3, \quad \mathbf{k}_{M3} = \pi\mathbf{G}^1 + \pi\mathbf{G}^3. \tag{4.4}$$

For each of these wave vectors there are six phonon modes, and at point $\mathscr{B}$ $(\theta = 0.97)$ the frequency for two of these modes is zero. This double eigenvalue corresponds to one longitudinal phonon mode (with atomic motion along the wave vector) and one transverse phonon mode (with atomic motion perpendicular to the wave vector). Thus, there are six simultaneous zero phonon frequencies, two for each of the three above wave vectors at $\theta = 0.97$ (point $\mathscr{B}$). For a comprehensive investigation of this multiple bifurcation point a 16-lattice corresponding to a $2 \times 2 \times 2$ block of $B2$ unit cells would need to be considered. This 51 DOF model would pose a formidable analytical and computational challenge. However, the three critical wave vectors (4.4) are related by symmetry, and thus, an analysis of only one of the three (say $\mathbf{k}_{M1}$) is necessary (see Fig. 10(a)).

The two critical eigen-modes (corresponding to Eq. (3.10) with $\omega = 0$ and normalized such that $\sum_\alpha \Delta \overset{(i)}{\widehat{\mathbf{v}}} \left[{}^{\mathbf{k}_{M1}}_{\alpha}\right] \bullet \Delta \overset{(i)}{\widehat{\mathbf{v}}} \left[{}^{\mathbf{k}_{M1}}_{\alpha}\right] = 1$, $i = 1, 2$) are given by

$$\Delta \overset{(1)}{\widehat{\mathbf{v}}} \begin{bmatrix} \mathbf{k}_{M1} \\ 0 \end{bmatrix} = 0.482\mathbf{G}_1 - 0.482\mathbf{G}_2, \quad \Delta \overset{(1)}{\widehat{\mathbf{v}}} \begin{bmatrix} \mathbf{k}_{M1} \\ 1 \end{bmatrix} = 0.403\mathbf{G}_1 - 0.403\mathbf{G}_2, \tag{4.5}$$

and

$$\Delta \overset{(2)}{\widehat{\mathbf{v}}} \begin{bmatrix} \mathbf{k}_{M1} \\ 0 \end{bmatrix} = 0.482\mathbf{G}_1 + 0.482\mathbf{G}_2, \quad \Delta \overset{(2)}{\widehat{\mathbf{v}}} \begin{bmatrix} \mathbf{k}_{M1} \\ 1 \end{bmatrix} = -0.403\mathbf{G}_1 - 0.403\mathbf{G}_2, \tag{4.6}$$

where the wavelength of these modes is $\lambda = \sqrt{2}a$. The first critical mode, $\Delta \overset{(1)}{\widehat{\mathbf{v}}} \left[{}^{\mathbf{k}_{M1}}_{\alpha}\right]$, shown in Fig. 10(b) is a transverse plane wave that shifts every other plane of atoms in a direction
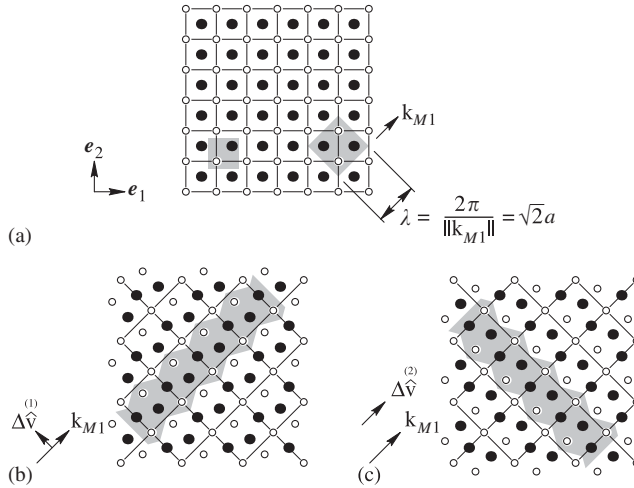
Fig. 10. Critical perturbation modes associated with critical wave vector $\mathbf{k}_{M1}$: (a) critical wave direction and wavelength; (b) transverse wave critical mode; (c) longitudinal wave critical mode.

perpendicular to the wave vector. The second critical mode, $\Delta \overset{(2)}{\widehat{\mathbf{v}}} \begin{bmatrix} \mathbf{k}_{M1} \\ \alpha \end{bmatrix}$, shown in Fig. 10(c) is a longitudinal plane wave where every other plane of atoms parallel to the wave vector shifts along the wave vector.

The 2-lattice description used so far cannot accommodate these perturbation modes as equilibrium configurations within the CB kinematics, and therefore, a description based on a larger unit cell, with more DOFs, must be introduced. Since the rightmost shaded region in Fig. 10(a) encompasses four atoms (and the wave vector has no component in the out of plane $\mathbf{e}_3$ direction) a 4-lattice description is likely needed to capture this mode within CB kinematics. Therefore, this larger M-lattice description is needed to follow bifurcated paths emerging from point $\mathscr{B}$. This suggests a numerical procedure as outlined in the next section.

4.4. Determining all connected, commensurate equilibrium paths

Whenever the phonon-stability criterion reaches a critical point where the intersecting equilibrium paths are not expressible under the multilattice description in use, a more general (larger M) multilattice description is required to investigate these paths. Thus, a systematic procedure is needed to investigate all commensurate equilibrium paths that are connected to the principal path. Starting with a chosen M-lattice description, the CB equilibrium configurations are identified for a single path. Next, all critical points along the path are classified as limit-loads, CB bifurcation points, or phonon bifurcation points. For CB bifurcation points the asymptotic analysis of Section 3.4.2 is employed to determine all emerging new paths. For phonon bifurcation points an investigation of the critical phonon modes suggests a new M-lattice description and the asymptotic analysis of Section 3.4.2 is then applied at the phonon bifurcation point to identify new bifurcating CB equilibrium paths. This procedure is summarized in Table 2.

Table 2
Procedure for determining all commensurate equilibrium paths connected to the principal path

(I) Choose an M-lattice description for the crystal.
(II) Determine CB-equilibrium configurations along a single path using the incremental Newton–Rhapson/Riks method.
(III) Identify all critical points that are encountered and refine their temperature and DOFs with the bi-section method.
(IV) Identify the type of critical point as limit-load, CB bifurcation, or phonon bifurcation.
   (a) Do nothing for limit-load points.
   (b) For CB bifurcation points do the following:
      (i) Evaluate $\mathscr{E}_{IJK}$ and $\mathscr{E}_{IJ\theta}$. If $\mathscr{E}_{IJK}$ is identically zero, go to Step IVb.iii.
      (ii) Solve bifurcation equation $(3.21)_1$ for $\boldsymbol{\alpha}$ and θ_1. If $\theta_1 = 0$ (a symmetric bifurcation) continue to Step IVb.iii, otherwise (asymmetric bifurcation) go to Step IVb.v.
      (iii) Evaluate $\mathbf{V}^{(IJ)}$ and $\mathscr{E}_{IJKL}$.
      (iv) Solve bifurcation Eq. $(3.21)_2$ for $\boldsymbol{\alpha}$ and θ_2.
      (v) (optional) Determine the initial CB-stability of each bifurcating branch using Eqs. (3.23).
   (c) For each commensurate phonon bifurcation point do the following:
      (i) Determine the associated modes and their wavelengths. Use this information to identify a new, larger, unit cell for the crystal.
      (ii) Choose a new M-lattice description for the crystal, thus rendering the phonon bifurcation point a CB bifurcation point of the new M-lattice. Go to Step IVb.
(V) Use the asymptotic results of Step IVb above and Eq. (3.19) to produce initial guesses for DOFs in the incremental Newton–Rhapson/Riks procedure for the newly identified equilibrium paths. Go to Step II.

5. Numerical results for a 4-lattice

The 4-lattice description of the $B2$ crystal structure is depicted in Fig. 11(a). The lattice correspondence between the 4-lattice unit cell (xyz) and the previous cubic frame (123) is shown in Fig. 11(b). This CB kinematic description has 15 degrees of freedom corresponding to six components of the uniform right stretch tensor $\mathbf{U}$ and nine components of the three internal shift vectors $\mathbf{S}[1], \mathbf{S}[2], \mathbf{S}[3]$. The reference lattice vectors, oriented at 45° to the original cubic basis $\mathbf{G}_1$, $\mathbf{G}_2$, $\mathbf{G}_3$, are

$$\mathbf{G}_x = \mathbf{G}_1 + \mathbf{G}_2, \quad \mathbf{G}_y = -\mathbf{G}_1 + \mathbf{G}_2, \quad \mathbf{G}_z = \mathbf{G}_3. \tag{5.1}$$

The reference position vectors are

$$\mathbf{X}\begin{bmatrix} \ell \\ \alpha \end{bmatrix} = \mathbf{X}[\ell] + \mathbf{P}[\alpha],$$

$$\mathbf{X}[\ell] \equiv \ell^x \mathbf{G}_x + \ell^y \mathbf{G}_y + \ell^z \mathbf{G}_z,$$

$$\mathbf{P}[0] \equiv \mathbf{0}, \quad \mathbf{P}[1] \equiv \tfrac{1}{2}\mathbf{G}_x + \tfrac{1}{2}\mathbf{G}_z,$$

$$\mathbf{P}[2] \equiv \tfrac{1}{2}\mathbf{G}_x + \tfrac{1}{2}\mathbf{G}_y, \quad \mathbf{P}[3] \equiv \tfrac{1}{2}\mathbf{G}_y + \tfrac{1}{2}\mathbf{G}_z, \tag{5.2}$$

and the current position vectors are given by

$$\mathbf{x}\begin{bmatrix} \ell \\ \alpha \end{bmatrix} = \mathbf{U} \bullet \left(\mathbf{X}\begin{bmatrix} \ell \\ \alpha \end{bmatrix} + \mathbf{S}[\alpha] \right),$$

$$\mathbf{S}[\alpha] \equiv S^x[\alpha]\mathbf{G}_x + S^y[\alpha]\mathbf{G}_y + S^z[\alpha]\mathbf{G}_z, \quad \alpha = 0, 1, 2, 3; \tag{5.3}$$

where again $\mathbf{S}[0] = \mathbf{0}$ is enforced to eliminate rigid-body translation modes.
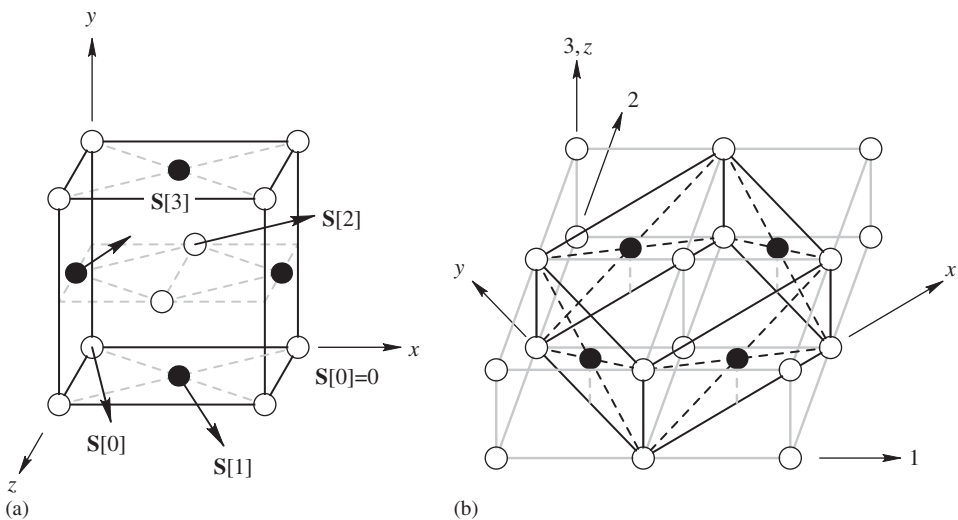

Fig. 11. Four-lattice model: (a) xyz tetragonal coordinate system; (b) 123 cubic coordinate system.

5.1. Stress-free equilibrium paths—phonon-stability

A stress-free energy density Eq. (3.3) is constructed as discussed in Section 3 with the 4-lattice description and the interaction potentials Eq. (3.13). The equilibrium equations (3.4) (where now $\alpha = 1, 2, 3$) are solved using the methods of Section 3.4.2 and the resulting bifurcation diagrams are displayed in Figs. 12–16.

The U_{zz} component of the right stretch tensor (with respect to an orthonormal basis aligned with the xyz frame) as a function of the dimensionless temperature θ is plotted in Fig. 12(a) for the range $0.3 < \theta < 5.5$, and Fig. 12(b) provides a magnified view of the region in the neighborhood of the critical point $\mathscr{B}$. As in the 2-lattice case, the cubic $B2$ equilibrium path is phonon-stable for high temperatures and phonon-unstable below the bifurcation point $\mathscr{B}$. The phonon-unstable tetragonal $L1_0$ equilibrium path is also shown. Point $\mathscr{B}$ corresponds to a multiple bifurcation point within the 4-lattice CB description, and an LSK analysis (see Elliott, 2004) determines that four symmetric stress-free equilibrium paths emerge from $\mathscr{B}$. There are two paths of a $B19$ orthorhombic crystal
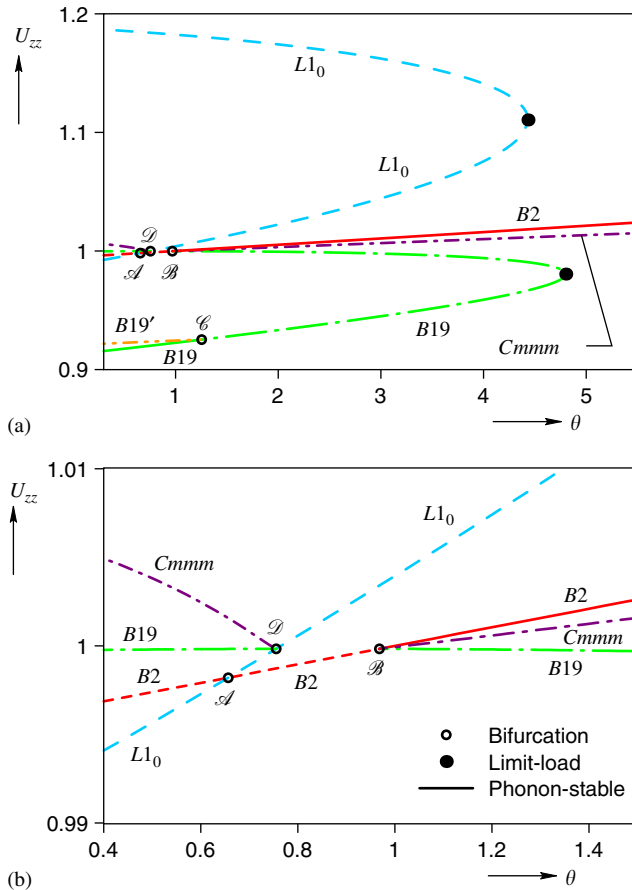
Fig. 12. Calculated 4-lattice stress-free equilibrium bifurcation diagrams showing the U_{zz} component of the deformation: (a) large temperature range; (b) expanded temperature scale near critical point $\mathscr{B}$.

structure (only one of which is displayed in the figure) belonging to the *Pmma* space group and two paths of a base-centered orthorhombic crystal structure (again only one path is plotted) belonging to the *Cmmm* space group. See Appendix A.1 for a description of these crystal structures and a discussion concerning the number of ''crystallographic variants'' for each crystal. The LSK results predict that each path emerging from $\mathscr{B}$ is symmetric and CB-unstable in the neighborhood of the bifurcation point (Elliott, 2004). This is confirmed in Fig. 13, where the asymptotic expression for the internal shift component $S^x[2]$ and the temperature θ along the *B19* and *Cmmm* (see Elliott, 2004) paths are compared to the numerically determined equilibrium states (squares and triangles, respectively). As can be seen, the agreement between these calculations and the analytical asymptotic results is good, but only for a small range of $S^x[2]$ values (note the vertical scale of Fig. 13), and therefore, the range of validity of the asymptotic expansion is small.

As shown in Fig. 12(a) the *Cmmm* equilibrium path emerging from $\mathscr{B}$ is phonon-unstable for the entire temperature range shown. The *B19* equilibrium path is initially phonon-unstable and remains phonon-unstable as it traverses a limit-load near $\theta = 4.80$. Eventually it stabilizes for temperatures below the secondary bifurcation point $\mathscr{C}$ at $\theta = 1.25$. An LSK analysis (Elliott, 2004) performed at the bifurcation point $\mathscr{C}$ reveals the emergence of a single *B19′* monoclinic equilibrium path that belongs to the *P2/m* space group. Appendix A presents the geometric characteristics of this monoclinic equilibrium crystal structure. The *B19′* path bifurcates symmetrically from $\mathscr{C}$ and is CB-unstable in the neighborhood of the bifurcation point. The asymptotically determined internal shift component $S^y[2]$ near $\mathscr{C}$ (see Elliott, 2004) is plotted in Fig. 14 along with the numerically determined equilibrium states for the *B19′* crystal structure. The agreement between these calculations and the analytical asymptotic results is good, but only for a small range of $S^y[2]$ values. The monoclinic *B19′* path is found to be phonon-unstable for all temperatures shown in Fig. 12(a).

In Fig. 12(b) a secondary bifurcation point $\mathscr{D}$ on the $L1_0$ path at a temperature of $\theta = 0.76$ is identified. An LSK analysis similar to the one performed for point $\mathscr{B}$ shows that a second set of symmetric orthorhombic equilibrium paths (*B19* and *Cmmm*) emerge from $\mathscr{D}$ and they are CB-unstable in the neighborhood of point $\mathscr{D}$. In this case, both the *B19* and *Cmmm* equilibrium paths remain phonon-unstable for their entire temperature range.

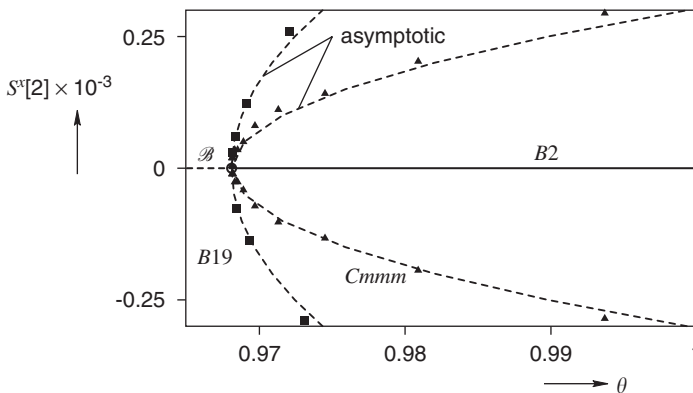
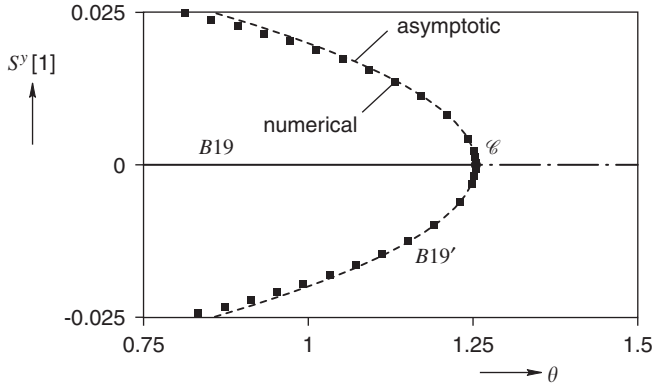Fig. 13. Asymptotic verification of numerical equilibrium states (squares = *B19*, triangles = *Cmmm*).

Fig. 14. Asymptotic verification of bifurcated $B19'$ ($P2/m$) orthorhombic equilibrium path.

The original set of orthorhombic $B19$ and *Cmmm* equilibrium paths initially emerge from point $\mathscr{B}$ by way of internal shifts of the atoms in the 4-lattice description. In Fig. 15 the internal shift components $S^x[1]$ and $S^x[3]$ are plotted as a function of temperature. The $B19$ and *Cmmm* paths are each symmetric about the horizontal zero line and both the $B2$ and $L1_0$ paths lie directly on this line since their internal shifts are identically zero. It is important to note the two orders of magnitude difference in the shifts $S^x[1]$ and $S^x[3]$ showing that atom 3 shifts within the unit cell by nearly 13% of the lattice spacing, whereas atom 1 shifts less than 0.5%.

The 4-lattice description has only two distinct stress-free equilibrium paths with phonon-stable segments, the $B2$ path attached to point $\mathscr{B}$ and the $B19$ path attached to point $\mathscr{C}$. Additionally, these segments satisfy CB-stability, and therefore, they are stable with respect to all quasi-uniform perturbations as well. The dimensionless energy density of these two paths and the unstable paths are plotted in Fig. 16(a). The stable segments of the $B2$ cubic and the $B19$ orthorhombic crystals overlap in temperature. Indeed, the $B19$ orthorhombic crystal structure stabilizes for temperatures below $\theta = 1.25$ (point $\mathscr{C}$), and the $B2$ cubic crystal structure is stable for temperatures above $\theta = 0.97$ (point $\mathscr{B}$). This suggests the existence of a hysteretic, temperature-induced, proper martensitic transformation cycle, as follows. Starting at high temperatures in the $B2$ cubic phase (austenite), the temperature is decreased until the $B2$ phase becomes unstable (at $\mathscr{B}$) and the material transforms to the stable $B19$ orthorhombic structure (martensite). If the temperature is now increased, the $B19$ crystal structure is initially stable, but destabilizes as the temperature reaches $\theta = 1.25$ (point $\mathscr{C}$). At this temperature the material undergoes the reverse transformation, returning to the original $B2$ crystal structure. Furthermore, the jump down in internal potential energy at $\mathscr{B}$ and the jump up in internal potential energy at $\mathscr{C}$ are consistent with the notion of exothermic and endothermic latent heat changes, respectively, that accompany such martensitic transformations.

Since the $B19$ structure has many energetically equivalent variants and its symmetry group is a proper subgroup of the $B2$ symmetry group (only one variant), this model has the potential to capture the shape memory effect. The change in volume $\Delta V/V = \det(\mathbf{U})$ with respect to the reference configuration as a function of temperature is shown in Fig. 16(b). The $B2$ cubic equilibrium path exhibits a nominally linear thermal expansion with a coefficient of linear thermal expansion (CTE) $\alpha = 17.4 \times 10^{-6}/\text{K}$ (as compared to the experimental value of $\alpha = 11 \times 10^{-6}/\text{K}$, Memry Corporation, 2004). The simulated
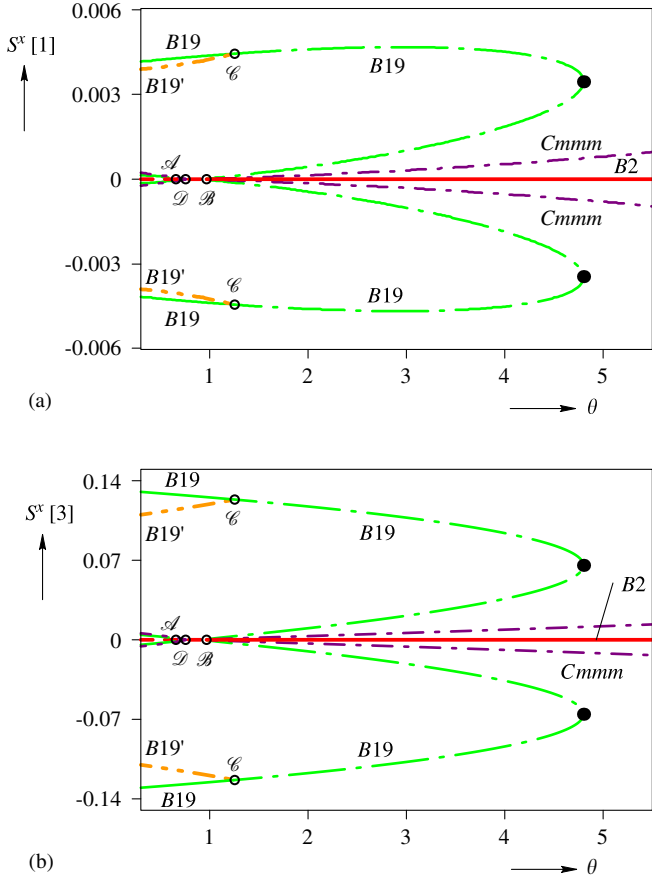
Fig. 15. Calculated 4-lattice stress-free equilibrium bifurcation diagrams showing: (a) the internal shift component $S^x[1]$ and (b) the internal shift component $S^x[3]$.

$B2 \rightarrow B19$ transformation at $\mathcal{B}$ has a 0.72% volume change, and the $B19 \rightarrow B2$ transformation at $\mathcal{C}$ has a -0.76% volume change. A third possible measure of the transformational volume change is given by the difference in volume between the $B2$ phase at $\theta_{\mathcal{C}}$ and the $B19$ phase at $\theta_{\mathcal{B}}$, which is -0.27%. These values are within the range of -0.139% to 0.820% reported in Table 9.2 of Bhattacharya (2003) for 12 different SMA's. As can be seen from Fig. 16(b), the CTE's of austenite and martensite can play an important role in the determination of the reported volume change, depending on the details of the particular experimental procedure. We choose to report the jump in deformation at a fixed temperature. The calculated transformation parameters at $\mathcal{B}$ (with respect to an orthonormal basis aligned with the $B19$ xyz frame) are

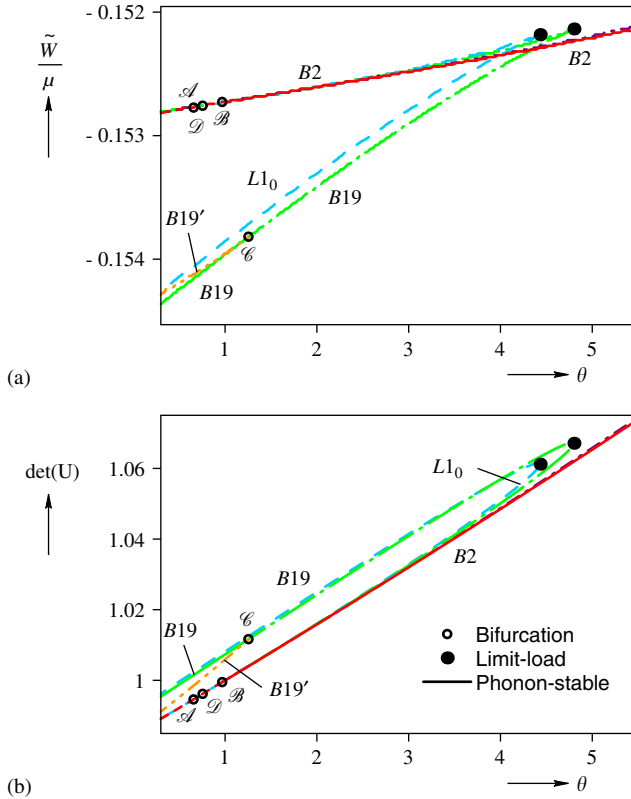$$\mathbf{U}^* = \begin{bmatrix} 1.0625 & 0 & 0 \\ 0 & 1.0277 & 0 \\ 0 & 0 & 0.9224 \end{bmatrix}, \tag{5.4}$$

Fig. 16. Calculated 4-lattice stress-free equilibrium bifurcation diagrams showing: (a) the dimensionless energy density $\tilde{W}/\mu$ versus dimensionless temperature; and (b) the change in volume with dimensionless temperature.

where $\mathbf{U}^*$ is defined by the relation $\mathbf{U}_{B19}(\theta_{\mathscr{B}}) = \mathbf{U}^* \cdot \mathbf{U}_{B2}(\theta_{\mathscr{B}})$. In the case of NiTi the transformation parameters are (Otsuka et al., 1971)

$$\mathbf{U}^*_{\text{NiTi}} = \begin{bmatrix} 1.0823 & 0 & 0.0603 \\ 0 & 0.9663 & 0 \\ 0.0603 & 0 & 0.9563 \end{bmatrix}, \tag{5.5}$$

(with principal values of 1.1065, 0.9663, and 0.9321) for which there is only modest agreement with the calculated transformation. This is expected since NiTi transforms between $B2$ and monoclinic $B19'$ (space group $P2_1/m$). We suspect that more sophisticated atomic potentials, with some angular dependence, such as 3-body potentials, would be required to model a stable crystal with such a low degree of symmetry as monoclinic. Better agreement, however, is obtained for other SMA's, such as AuCd (Chang and Read, 1951) and CuAlNi (Otsuka and Shimizu, 1974), both of which exhibit a proper martensitic transformation similar to $B2 \rightarrow B19$. These transformation

parameters are

$$\mathbf{U}^*_{\text{AuCd}} = \begin{bmatrix} 1.0350 & 0 & 0 \\ 0 & 1.0138 & 0 \\ 0 & 0 & 0.9491 \end{bmatrix}, \quad \mathbf{U}^*_{\text{CuAlNi}} = \begin{bmatrix} 1.0619 & 0 & 0 \\ 0 & 1.0231 & 0 \\ 0 & 0 & 0.9178 \end{bmatrix}.$$

(5.6)

The agreement between the calculated and experimental transformation parameters is reasonable for AuCd and is surprisingly good for the pseudo-binary alloy CuAlNi.

6. Summary and conclusions

A set of temperature dependent, nonlocal, atomic pair-potentials is used to derive a thermo-elastic energy density to simulate the bulk mechanical behavior of a prototype bi-atomic crystal. The aim is to model crystal instabilities that are the underlying mechanism for martensitic transformations which occur in shape memory alloys (SMA's). Atomic degrees of freedom (DOFs) are described by a multilattice using CB kinematics, which include a uniform deformation gradient and internal shifts of sub-lattices. Stress-free equilibrium paths are found numerically, and stability of each is evaluated using a combination of the CB-stability criterion and the phonon-stability criterion according to the approach recommended by the companion paper Elliott et al. (2004b) (Part I). Additionally, a general procedure is identified for determining all commensurate equilibrium paths that are connected to the crystal's principal path.

Initially, a 2-lattice description is used to describe a $B2$ crystal, which is a common crystal structure of the austenite phase in SMA's. Using a set of Morse pair-potentials, where the bonds' natural lengths increase with temperature, results in the $B2$ crystal having a principal branch that is stable at high temperatures but CB-unstable at low temperatures. An asymptotic analysis at the critical point identifies a set of transcritically intersecting equilibrium paths corresponding to the variants of a tetragonal crystal ($L1_0$ structure). According to the CB-stability criterion this secondary branch is initially unstable, but then stabilizes as it crosses a ''limit-load'' (actually ''limit-temperature'', the loading parameter), resulting in overlapping stable segments between the principal and secondary branches. However, the entire tetragonal branch is subsequently shown to be unstable with respect to the phonon-stability criterion and the onset of phonon-instability upon cooling along the primary branch actually occurs sooner (at a higher temperature). These results underscore the importance of using both the CB- and phonon-stability criteria to establish the stability of such a multi-lattice, since they ensure stability with respect to complementary types of perturbations, i.e., quasi-uniform perturbations of infinite wavelength (CB) and bounded perturbations of all finite wavelengths (phonon).

An investigation of the critical modes of the ''new'' (phonon) bifurcation point then leads to the study of a 4-lattice. The larger number of DOFs allows a set of symmetric intersecting equilibrium branches to emerge from this new bifurcation point. While many other unstable crystal structures are shown to exist, a set of secondary branches emerge from the phonon bifurcation point that correspond to an orthorhombic crystal ($B19$ structure), which is initially unstable, undergoes a ''limit-load'', and then stabilizes (both

CB and phonon criteria) for temperatures below a secondary bifurcation point. This bifurcation point occurs at a higher temperature than the primary bifurcation point, leaving overlapping stable segments of the $B2$ (austenite) equilibrium path at high temperatures and the $B19$ (martensitic) paths at low temperatures. This indicates the presence of a hysteretic temperature-induced proper martensitic transformation. The most prevalent bi-atomic SMA is NiTi, which has a $B2$ austenite and a monoclinic $B19'$ martensite. Our calculations show $B19'$ paths that bifurcate from the $B19$ branch, but they are predicted to be unstable. We suspect this is due to the simple central-force potentials used in the calculations. However, certain other SMA's do exhibit martensitic transformations from $B2$ to $B19$ (AuCd), or at least between cubic to orthorhombic lattices (CuAlNi). The predicted jump in deformation gradient components compare favorably with experimentally obtained values for AuCd and CuAlNi.

These successful results indicate a promising avenue for future study of SMA's at the atomic scale. For the first time, an atomic-scale calculation has been used to simulate the equilibrium paths and their changes in stability consistent with temperature-induced martensitic transformations seen in SMA's. The group–subgroup relationship between the austenite ($B2$) and martensite ($B19$) crystal symmetries indicates that a shape memory behavior is possible. The effect of an applied stress still needs to be evaluated before shape memory behavior and pseudoelasticity can be demonstrated, but this will be addressed in future work. The ultimate realization of such a model should provide a useful numerical tool to answer fundamental questions at the atomic scale regarding the origins of shape memory behavior and nano-scale structure evolution.

Acknowledgments

Appendix A

A.1. Crystal structure determination

The LSK asymptotic techniques of Section 3.2 determine the equilibrium paths which emerge from a bifurcation point, but they provide little help in identifying the symmetry of the resulting crystal structures. For this, the computer program *MS Modeling* created by Accelrys (2004) is used by supplying it with atomic positions within the crystal at some arbitrary point along the equilibrium path of interest (away from any bifurcation points, where the symmetry of the crystal often becomes degenerate). The program's *find symmetry* function is then used to perform a regression analysis on these atomic positions and determine the largest space group to which the crystal belongs. Another, freely
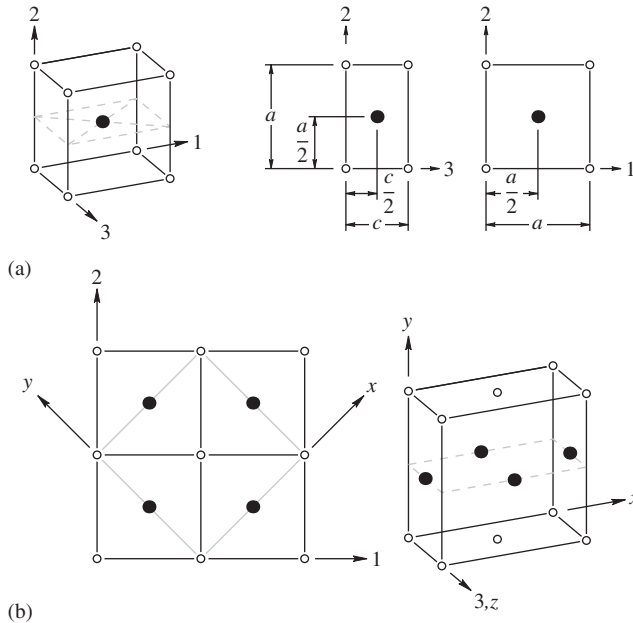
Fig. A.1. $L1_0$ ($P4/mmm$) tetragonal crystal structure: (a) primitive unit cell geometry; (b) larger conventional unit cell.

available, program for accomplishing this task is *ISOTROPY* developed by Stokes and Hatch (2002).

The $L1_0$ (space group $P4/mmm$) crystal structure is shown in Fig. A.1(a) and is completely determined by the two lattice parameters a and c. Fig. A.1(b) displays the correspondence between the primitive unit cell of the $L1_0$ crystal structure and the larger more conventional unit cell containing four atoms (see US NRL Center for Computational Materials Science, 2004). When $a = c$ the $L1_0$ crystal becomes the $B2$ cubic crystal structure. The $L1_0$ equilibrium path, plotted in Fig. 5, is characterized within the 2-lattice CB kinematics by the right stretch tensor

$$\mathbf{U} = \begin{bmatrix} a & 0 & 0 \\ 0 & a & 0 \\ 0 & 0 & c \end{bmatrix}, \tag{A.1}$$

in the 123 frame of Fig. 2, and the internal shift is zero

$$\mathbf{S} = \mathbf{0}. \tag{A.2}$$

The geometry of the $B19$ (space group $Pmma$) crystal structure is shown in Fig. A.2(a) and is completely determined by the three lattice parameters a, b, and c and the two "motif parameters" ζ_1 and ζ_2 (see US NRL Center for Computational Materials Science, 2004). When $a = b = \sqrt{2}c$ and $\zeta_1 = \zeta_2 = a/4$ the $B19$ structure reduces to the $B2$ crystal. When $a = b \neq \sqrt{2}c$ and $\zeta_1 = \zeta_2 = a/4$ it reduces to the $L1_0$ structure. The correspondence between the $B19$ primitive unit cell and the 4-lattice unit cell (with atoms located at the corners) used in the calculations of Section 4 is shown in Fig. A.2(b). As can be seen,
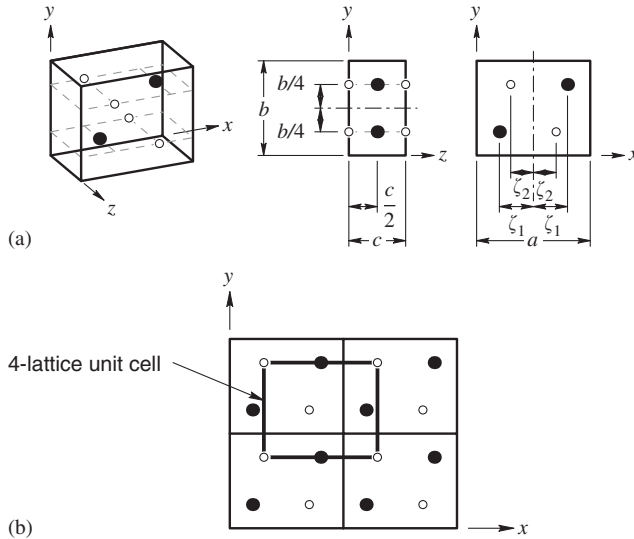
Fig. A.2. *B*19 (*Pmma*) orthorhombic crystal structure: (a) primitive unit cell geometry; (b) 4-lattice unit cell with atoms located at the corners.

the 4-lattice unit cell obscures much of the symmetry of the motif; whereas, the primitive unit cell of Fig. A.2(a) clearly displays the simple relationships defining the *B*19 crystal structure. This appears to be a general observation, i.e., the symmetry of a crystal's motif is often obscured by placing atoms at the corners of the unit cell (except for the cubic crystals). Further examples of this are found in the *Cmmm* and *B*19′ crystal structures. The *B*19 equilibrium path (depicted in Fig. 12) is characterized within the 4-lattice CB kinematics by a uniform deformation of the form

$$\mathbf{U} = \begin{bmatrix} a & 0 & 0 \\ 0 & b & 0 \\ 0 & 0 & c \end{bmatrix} \tag{A.3}$$

with respect to the *xyz* frame, and it occurs as a higher-order effect coupled to the shifts. The internal shifts obey the relations[8]

$$S^x[3] = S^x[2] - S^x[1],$$
$$S^y[\alpha] = S^z[\alpha] = 0, \quad \alpha = 1, 2, 3. \tag{A.4}$$

Thus, the atoms 1, 2, and 3 remain in their initial *xz* plane and shift in the *x* direction.

There are generally understood to be six variants of an orthorhombic crystal structure originating from a cubic austenite phase (see, for example Bhattacharya, 2003). Indeed, in the current case there are two orthorhombic equilibrium paths that emerge from bifurcation point $\mathscr{B}$ when one considers the wave vector $\mathbf{k}_{M1}$ (see Section 4.3). If the two

---

[8]Note that a misprint of these shift relations occurred in Eq. (25) of the paper Elliott et al. (2004a) which is corrected in Eq. $(A.4)_1$.
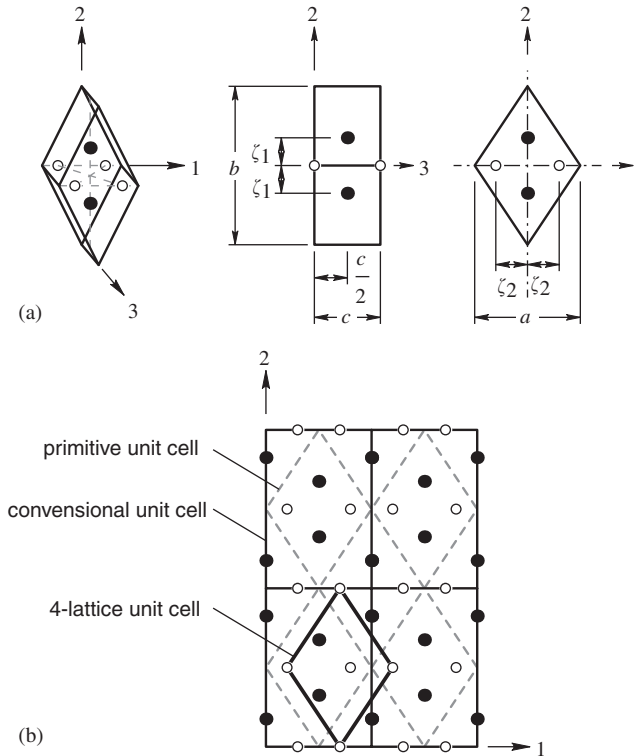
Fig. A.3. *Cmmm* base-centered orthorhombic crystal structure: (a) primitive unit cell geometry; (b) conventional orthogonal unit cell and primitive unit cell with atoms located at the corners.

wave vectors $\mathbf{k}_{M2}$ and $\mathbf{k}_{M3}$ are included one finds that each of these add two orthorhombic variants of their own, and thus, the expected six variants of the orthorhombic phase are obtained. It is interesting to note that when the full crystallographic details of the structure are taken into account, this definition of the variants of a martensite phase is inadequate. In fact, there are 12 distinct "crystallographic variants" of the orthorhombic $B19$ crystal structure, that is, there are two variants of the crystal structure associated with each equilibrium path such as the ones emerging from $\mathcal{B}$. Each side of the symmetric bifurcation path shown in Fig. 15 corresponds to a distinct variant of the $B19$ crystal structure and these two variants are related through a 180° rotation about the y axis. These "extra" variants are related to the concepts of *merohedral-twinning* or *motif-twinning* and *shuffle-twinning* (also called *antiphase boundaries*, see Phillips, 2001) which are briefly discussed by Pitteri and Zanzotto (2002).

The base-centered orthorhombic *Cmmm* primitive unit cell is displayed in Fig. A.3(a). This crystal structure is completely determined by the three lattice parameters a, b, and c and the two motif parameters ζ_1 and ζ_2. When $a = b = \sqrt{2}c$ and $\zeta_1 = \zeta_2 = a/4$ the structure becomes the $B2$ cubic crystal. Fig. A.3(b) shows the correspondence between the *Cmmm* primitive unit cell of Fig. A.3(a), the conventional base-centered unit cell, and the correspondence with the 4-lattice unit cell (with atoms located at its corners) used in the calculations. The *Cmmm* equilibrium path (shown in Fig. 12) is characterized within
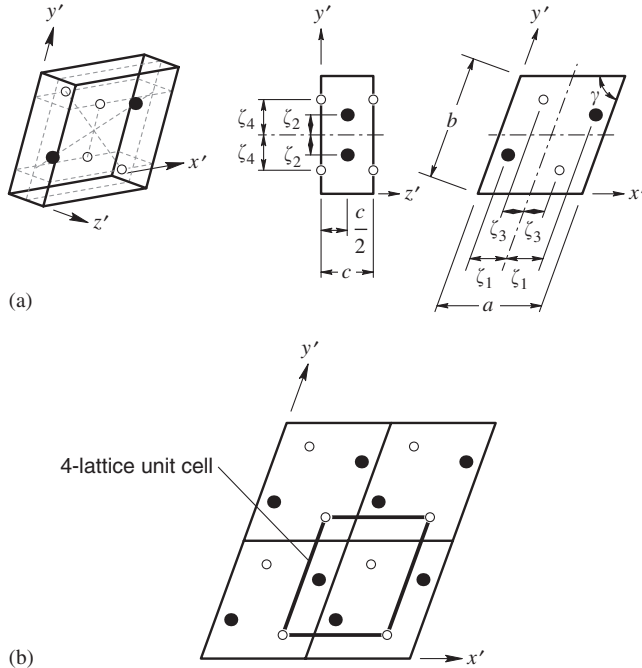
Fig. A.4. $B19'$ ($P2/m$) monoclinic crystal structure: (a) primitive unit cell geometry; (b) unit cell with atoms located at the corners.

the 4-lattice CB kinematics by a uniform deformation of the form

$$
\mathbf{U} = \begin{bmatrix} \dfrac{a+b}{2} & \dfrac{a-b}{2} & 0 \\ \dfrac{a-b}{2} & \dfrac{a+b}{2} & 0 \\ 0 & 0 & c \end{bmatrix},
\tag{A.5}
$$

with respect to the xyz frame, and the internal shifts obey the relations[9]

$$S^x[2] = S^y[2] = S^x[1] + S^y[1],$$

$$S^x[3] = S^y[1],$$

$$S^y[3] = S^x[1],$$

$$S^z[\alpha] = 0, \quad \alpha = 1, 2, 3.
\tag{A.6}$$

The $B19'$ (space group $P2/m$) crystal structure is shown in Fig. A.4(a) where the monoclinic primitive unit cell is displayed. This structure is uniquely defined by the four lattice parameters a, b, c, and γ and the four motif parameters ζ_1, ζ_2, ζ_3, and ζ_4. When $\gamma = 90°$ and $\zeta_2 = \zeta_4 = b/2$ the $B19'$ structure becomes a $B19$ crystal. Fig. A.4(b) shows the

---

[9]Note that a misprint of these shift relations occurred in Eq. (26) of the paper Elliott et al. (2004a) which is corrected in Eq. (A.6)$_1$.

correspondence between the $B19'$ primitive unit cell and the 4-lattice unit cell (with atoms located at its corners) used in the calculations. The $B19'$ equilibrium path is characterized within the 4-lattice CB kinematics by a uniform deformation of the form

$$\mathbf{U} = \begin{bmatrix} a & \gamma & 0 \\ \gamma & b & 0 \\ 0 & 0 & c \end{bmatrix}, \tag{A.7}$$

with respect to the xyz frame, and the internal shifts are constrained to satisfy the relations

$$S^x[3] = S^x[2] - S^x[1],$$

$$S^y[3] = S^y[2] - S^y[1],$$

$$S^z[\alpha] = 0, \quad \alpha = 1, 2, 3. \tag{A.8}$$

References

Abeyaratne, R., Knowles, J.K., 1993. A continuum model of a thermoelastic solid capable of undergoing phase transitions. J. Mech. Phys. Solids 41 (3), 541–571.

Accelrys, 2004. MS modeling. http://www.accelrys.com.

Ahluwalia, R., Lookman, T., Saxena, A., Albers, R.C., 2004. Landau theory for shape memory polycrystals. Acta Materialia 52 (1), 209–218.

Beatty, M.F., Hayes, M.A. (Eds.), 2005. Mechanics and Mathematics of Crystals: Selected Papers of J.L. Ericksen, first ed. World Scientific, Singapore.

Bhattacharya, K., 1991. Wedge-like microstructure in martensites. Acta Metallurgical et Materialia 39 (10), 2431–2444.

Bhattacharya, K., 2003. Microstructure of martensite: why it forms and how it gives rise to the shape-memory effect. Oxford Series on Materials Modelling, first ed. Oxford University Press, Oxford.

Born, M., Huang, K., 1962. Dynamical Theory of Crystal Lattices, first ed. Oxford University Press, Oxford.

Boyd, J.G., Lagoudas, D.C., 1994. Constitutive model for simultaneous transformation and reorientation in shape memory materials. Am. Soc. Mech. Eng., Appl. Mech. Div., AMD. Mech. Phase Transform. Shape Memory Alloys. 189, 159–172.

Brinson, L.C., 1993. One-dimensional constitutive behavior of shape memory alloys: thermomechanical derivation with non-constant material functions and redefined martensite internal variable. J. Intel. Mater. Systems Struct. 4, 229–242.

Brown, I.D., Dabkowski, A., McCleary, A., 1997. Thermal expansion of chemical bonds. Acta Crystallogr. Sect. A 52, 750–761.

Bruce, A.D., Cowley, R.A., 1981. Structural Phase Transitions. Monographs on Physics. Taylor & Francis, London.

Carlsson, A.E., 1990. Solid State Physics, vol. 43. Academic Press, New York, pp. 1–91 (Chapter–Beyond Pair Potentials in Elemental Transition Metals and Semiconductors).

Chang, L.C., Read, T.A., 1951. Plastic deformation and diffusionless phase changes in metals—the gold–cadmium beta phase. Am. Inst. Min. Metall. Eng.—J. Met. 191 (1), 47–52.

Charlotte, M., Truskinovsky, L., 2002. Linear elastic chain with a hyper-prestress. J. Mech. Phys. Solids 50 (2), 217–251.

Chu, C., James, R.D., 1995. Analysis of microstructures in Cu-14.0%Al-3.9%Ni by energy minimization. J. Phys. C8 5, 143–149.

Cohen, M., Olson, G.B., Clapp, P.C., 1979. On the classification of displacive phase transformations. In: Proceedings of ICOMAT-79, p. 1. International Conference on Martensitic Transformations.

Dove, M.T., 1993. Introduction to Lattice Dynamics. Cambridge University Press, Cambridge.

Elliott, R.S., 2004. Lattice-level instabilities in bi-atomic alloys. Ph.D. Thesis, Department of Aerospace Engineering, The University of Michigan, Ann Arbor, MI, USA.

Elliott, R.S., Shaw, J.A., Triantafyllidis, N., 2002a. Stability of pressure-dependent, thermally-induced displacive transformations in bi-atomic lattices. Int. J. Solids Struct. 39 (13–14), 3845–3856.

Elliott, R.S., Shaw, J.A., Triantafyllidis, N., 2002b. Stability of thermally-induced martensitic transformations in bi-atomic crystals. J. Mech. Phys. Solids 50 (11), 2463–2493.

Elliott, R.S., Shaw, J.A., Triantafyllidis, N., 2004a. Stability of dispersive bi-atomic crystals. In: Lagoudas, D.C. (Ed.), Smart Structures and Materials 2004: Active Materials: Behavior and Mechanics, Proceedings of SPIE, vol. 5387. The International Society for Optical Engineering (SPIE), pp. 239–248.

Elliott, R.S., Triantafyllidis, N., Shaw, J.A., 2004b. Stability of crystalline solids—I: Continuum and atomic-lattice considerations. J. Mech. Phys. Solids, submitted for publication, doi:10.1016/j.mps.2005.07.009.

Ericksen, J.L., 1975. Equilibrium of bars. J. Elasticity 5 (3–4), 191–201.

Ericksen, J.L., 1978. On the symmetry and stability of thermoelastic solids. J. Appl. Mech.—Transact. ASME 45, 740–744.

Ericksen, J.L., 1984. Phase Transformations and Material Instabilities in Solids. Academic Press, New York, pp. 61–77 (Chapter: The Cauchy and Born Hypotheses for Crystals).

Ericksen, J.L., 1992. Bifurcation and martensitic transformations in bravais lattices. J. Elasticity 28, 55–78.

Fukuda, T., Kakeshita, T., Houjoh, H., Shiraishi, S., Saburi, T., 1999. Electronic structure and stability of intermetallic compounds in the Ti–Ni system. Mater. Sci. Eng. 273–275, 166–169.

Girifalco, L.A., Weizer, V.G., 1959. Application of the morse potential function to cubic metals. Phys. Rev. 114 (3), 687–690.

Grujicic, M., Dang, P., 1995. Computer simulation of martensitic transformation in Fe-Ni face-centered cubic alloys. Mater. Sci. Eng. A201 (1–2), 194–204.

Hall, G.J., Govindjee, S., 2002. Application of a partially relaxed shape memory free energy function to estimate the phase diagram and predict global microstructure evolution. J. Mech. Phys. Solids 50 (3), 501–530.

Hane, K.F., Shield, T.W., 1999. Microstructure in the cubic to monoclinic transition in titanium-nickel shape memory alloys. Acta Materialia 47 (9), 2603–2617.

Huang, X., Bungaro, C., Godlevsky, V., Rabe, K.M., 2002. Lattice instabilities of cubic NiTi from first principles. Phys. Rev. B: Condensed Matter 65(1), 014108/1–5.

James, R.D., 1986. Displacive phase transformations in solids. J. Mech. Phys. Solids 34 (4), 359–394.

Kastner, O., 2003. Molecular dynamics of a 2D model of the shape memory effect part i: model and simulations. Continuum Mech. Thermodyn. 15 (5), 487–502.

Leo, P.H., Shield, T.W., Bruno, O.P., 1993. Transient heat transfer effects on the pseudoelastic behavior of shape-memory wires. Acta Metall. et Mater. 41 (8), 2477–2485.

Levitas, V.I., 1998. Thermomechanical theory of martensitic phase transformations in inelastic materials. Int. J. Solids Struct. 35 (9–10), 889–940.

Melker, A.I., Ivanov, A.A., 2000. Temperature dependent potentials for molecular dynamics. In: Melker, A.I. (Ed.), Third International Workshop on Nondestructive Testing and Computer Simulations in Science and Engineering, vol. 4064, pp. 165–170 (Proceedings of SPIE, 2000).

Memry Corporation, 2004. NiTi frequently asked questions. http://www.memry.com/nitinolfaq/nitinolfaq.html.

Miller Jr., W., 1972. Symmetry Groups and Their Applications, first ed., vol. 50. Pure and Applied Mathematics. Academic Press, New York.

Ngan, S.-C., Truskinovsky, L., 1999. Thermal trapping and kinetics of martensitic phase boundaries. J. Mech. Phys. Solids 47 (1), 141–172.

Nye, J.F., 1985. Physical Properties of Crystals. Oxford University Press, Oxford.

Otsuka, K., Sawamura, T., Shimizu, K., 1971. Crystal structure and internal defects of equiatomic TiNi martensite. Phys. Status Solidi A 5 (2), 457–470.

Otsuka, K., Shimizu, K., 1974. Morphology and crystallography of thermoelastic Cu-Al-Ni martensite analyzed by the phenomenological theory. Trans. Japan Inst. Met. 15 (2), 103–108.

Patel, V.A., 1994. Numerical Analysis. Saunders College Publishing, Fort Worth.

Patoor, E., Eberhardt, A., Berveiller, M., 1996. Micromechanical modelling of superelasticity in shape memory alloys. J. Physi. IV: JP 6, C1–277–C1–292.

Phillips, R., 2001. Crystals Defects and Microstructures: Modeling Across Scales, first ed. Cambridge University Press, Cambridge.

Pitteri, M., 1984. Reconciliation of local and global symmetries of crystals. J. Elasticity 14, 175–190.

Pitteri, M., Zanzotto, G., 2002. Continuum Models for Phase Transitions and Twinning in Crystals, Applied Mathematics, vol. 19. Chapman & Hall, London.

Riks, E., 1979. Incremental approach to the solution of snapping and buckling problems. Int. J. Solids Struct. 15 (7), 529–551.

Sands, D.E., 1993. Introduction to Crystallography. Dover, New York.

Saxena, A., Ahluwalia, R., Lookman, T., Albers, R.C., 2003. Constitutive response of polycrystalline shape memory alloys. Mater. Sci. Forum 426–432 (3), 2255–2260.

Shao, Y., Clapp, P.C., Rifkin, J.A., 1996. Molecular dynamics simulation of martensitic transformations in NiAl. Metall. Transact. 27A (6), 1477–1489.

Shaw, J.A., 2002. A thermochemical model for a 1-D shape memory alloy wire with propagating instabilities. Int. J. Solids Struct. 39 (5), 1275–1305.

Shaw, J.A., Kyriakides, S., 1995. Thermomechanical aspects of NiTi. J. Mech. Phys. Solids 43 (8), 1243–1281.

Shaw, J.A., Kyriakides, S., 1997. On the nucleation and propagation of phase transformation fronts in a NiTi alloy. Acta Materialia 45 (2), 683–700.

Stokes, H.T., Hatch, D.M., 2002. ISOTROPY. http://stokes.byu.edu/isotropy.html.

Sun, Q.P., Hwang, K.C., 1993. Micromechanics modelling for the constitutive behavior of polycrystalline shape memory alloys. i. derivation of general relations. J. Mech. Phys. Solids 41 (1), 1–17.

Sutton, A.P., 1989. Temperature-dependent interatomic forces. Philos. Mag. 60 (2), 147–159.

Tanaka, K., 1986. Thermomechanical sketch of shape memory effect: one-dimensional tensile behavior. Int. J. Struct. Mech. Mater. Sci. 18 (3), 251–263.

Tolédano, P., Dmitriev, V., 1996. Reconstructive Phase Transitions. World Scientific, Singapore.

Torrens, I.M., 1972. Interatomic Potentials. Academic Press, New York.

Triantafyllidis, N., Peek, R., 1992. On stability and the worst imperfection shape in solids with nearly simultaneous eigenmodes. Int. J. Solids Struct. 29 (18), 2281–2299.

US NRL Center for Computational Materials Science, 2004. Crystal lattice structures web page. http://cst-www.nrl.navy.mil/lattice/.

Vainchtein, A., 1999. Dynamics of phase transformations and hysteresis in a viscoelastic ericksen's bar on an elastic foundation. J. Elasticity 57 (3), 243–280.

Wallace, D.C., 1998. Thermodynamics of Crystals. Dover, New York.

Yu, Z.-Z., Clapp, P.C., 1989. Growth dynamics study of the martensitic transformation in Fe–30 Pct Ni alloys. Part II. computer simulation of martensitic growth. Metall. Trans. 20A (9), 1617–1629.

Zarkova, L., 1996. An isotropic intermolecular potential with temperature dependent effective parameters for heavy globular gases. Mol. Phys. 88 (2), 489–495.